Receiver functions at the 8 broadband seismometers of the Kongsberg array

Mathilde Sofie Opshaug

Master's thesis in Geoscience
Geophysics Program
60 credits

Department of Geosciences
Faculty of Mathematics and Natural Science
UNIVERSITY OF OSLO
Norway
Spring 2020

Receiver functions at the 8 broadband seismometers of the Kongsberg array

by
Mathilde Sofie Opshaug

Receiver functions at the 8 broadband seismometers of the Kongsberg array

Supervisors: Prof. Valerie Maupin and Associate Prof. Johannes Schweitzer

http://www.duo.uio.no/

Printed: Reprosentralen, University of Oslo

Abstract

The P-Receiver functions(RFs) at 8 temporary seismic stations named KONO1 to KONO8, located in a 100x100 km region around Kongsberg (Norway) are analysed in this thesis. RFs use S converted waves arriving at the seismological station after the main P-wave, to detect impedance contrasts beneath the seismic station, and is utilized in particular to find Moho depth beneath a station. The stations used in this thesis, are placed within and outside of the Oslo Graben. The data are provided by the interactive database IRIS for the permanent station KONO, and NORSAR for the eight temporary stations(KONO1-8). 219 seismic events were selected within the time frame April 2018 to September 2019, of which 150 could be used to produce receiver functions of acceptable quality.

The results from the single receiver functions were analysed. We also stacked receiver functions from events in 3 regions(Japan, Philippines and Indonesia, Alaska and Canada) in order to enhance the signal-to-noise ratio and get a better view of the converted and reflected waves in the crust. This enables is to analyse how the RFs vary with the back azimuth of the source region. From this it is found that KONO4, KONO5, KONO6 and KONO8, which lies farthest away from KONO, gives similar RFs in different back azimuths. This means that all three stacking areas that are mainly used in this thesis can be further stacked together for each of these stations, to try and enhance the crustal arrivals and subsequently perform a formal inversion. While KONO1, KONO2 and KONO3, which lies closest to KONO, gives different RFs depending on their back azimuth and might indicate a dipping lower crustal layer, a dipping Moho, scattering of waves, anisotropy or structural heterogeneity. KONO1, KONO2, KONO3 and KONO4 show a negative arrival at 10s that was also found in previous studies. Based on the arrival time this might indicate the arrival of a PPmP, or may be a mantle reflection. KONO4 is however located further away from KONO, and the negative arrival is probably not caused by the same structure as at KONO, KONO1, KONO2 and KONO3. The Ps- wave has a high visibility at KONO, KONO1, KONO2 and KONO3, in the west, while the events arriving from the east display the PPmP-wave. This can be explained with a more complex Moho. However, KONO4 show strong arrivals of the Ps-wave in all directions, also the direction that displays PPmP-arrivals, and thereby indicates a more complicated structure.

Acknowledgements

I would like to thank my main supervisor, Prof. Valerie Maupin for letting me study such an interesting topic, for all the help, and motivating me through the feedback I got to improve this thesis. Would also like to thank my other supervisor Associate Prof. Johannes Schweitzer for the feedback and ideas surrounding this topic.

I would like to thank Annie Jerkins and Ulf Baadshaug for the information provided on the seismic stations and data for my thesis.

I would like to thank my study teammates Trine, Marcus and Helge for endless laughter and support, even though our time leading up to the deadline got a little different than what we expected. I big thank you to my friend, roomie and cousin Anne- Johanne for putting up with me, making me laugh and dragging me out from my master thesis for a breath of fresh air. Would also like to thank all my friends for the support, especially Guro and Peder that helped me with the grammar in my thesis.

Finally, I would like to thank my parents for the constant support and always being there with calming words, and giving me perspective when I need it. Thank you to my sister for the dinners, walks and always being there. And thank you to my brother for the support.

Contents

List of Figures

List of Tables

1 Introduction

Over the last three decades interpretation of converted waves and seismic tomography have been fundamental methods used to seismic image the Earth, both regionally and globally (Rondenay, 2009). A seismogram where the source signature of the earthquake and the instrument response from the seismic station have been removed, and thereby only shows the converted energy from the incident wave, is called a receiver function (Langston (1979): Sawade (2018)). Receiver functions was introduced about 40 years ago in the end of the 1970s by Vinnik (1977) and Langston (1979), where they used normalised signals of converted waves to image the impedance contrast within the Earth (Rondenay (2009): Frassetto and Thybo (2013)). Teleseismic body waves are mainly used, and the method is used for the study of the upper mantle (Burdick and Langston (1977): Owens et al. (1984): Kind et al. (1995)). To improve the signal-to-noise ratio multiple events can be stacked (Ryberg and Weber, 2000).

Receiver functions in Norway has been studied by Ottemöller and Midzi (2003), Frassetto and Thybo (2013) and Kolstrup and Maupin (2013), where receiver functions from KONO was looked at, along with other areas from different parts of Norway. They found that the receiver functions from KONO varied with the back azimuth and thereby indicated a more complicated structure underneath the station. The data therefore did not get put through a formal inversion to obtain the velocity model with depth. In addition, Marianne Kolstrup (unpublished), found anomalous arrivals in the receiver functions from KONO a few seconds after the S wave converted at the Moho. The arrival time of these anomalous waves corresponds to the PPmP wave, but this wave should in theory not appear on receiver functions. The events that showed these arrivals had a back azimuth between 0-90 degrees, and led to unrealistic low mantle velocities when calculating the mantle velocity using the standard 1D inversion technique. The purpose of placing the temporary stations within a 50 km radius was to get more data with a better geographical coverage, and find a reason for these arrivals. Teleseismic earthquakes will be used to recalculate the P-receiver functions from KONO, and to calculate P-receiver functions for each of the eight temporary seismic stations.

After this introduction, the geological background for the area around the seismic

station will be presented in chapter 2. Then in chapter 3, some theoretical background about the Earth structure and the propagating waves will be reviewed. Chapter 4 and 5 present the collection and preparation of the data, and the different processing steps taken to get receiver functions. The results are presented in chapter 6, where first single events and then stacked events are viewed, before looking at the conversion and reflection points. Chapter 7 will discuss the results and what they indicate. Lastly in chapter 8, a conclusion is provided as well as a the future outlook.

2 Geological background

KONO and the eight temporary stations are placed in different areas within and outside of the Oslo Graben, as seen in figure 1. The geological background is therefore different, and has to be explained separately to get a clear picture of the properties and conditions of the ground in the area where the seismic stations are placed. Because of this location, we expect lateral variations of the crust that could affect the P-receiver functions.

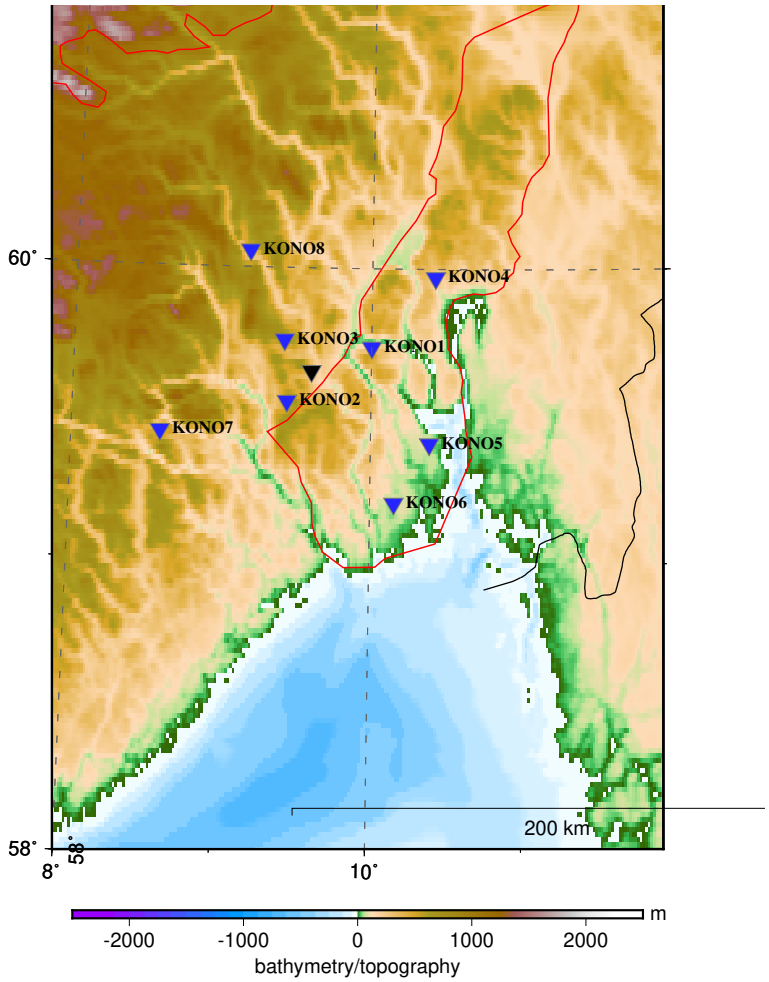

Figure 1: Map over the location of KONO (black triangle) and the eight temporary stations (blue triangle). The red lines shows the boundaries of the Oslo Graben.

The Oslo Graben consists of two main grabens called Akershus Graben and Vestfold Graben, and these are separated by the Krokskogen transfer zone, as seen in figure 4a

(Andersen et al., 2008). The geological significance of the Oslo Graben was already discovered over 200 years ago. From then until now this area have been mapped and studied by many different scientists, starting with the German geologist Leopold von Buch in the early 18th century (Ramberg et al., 2013).

This area has been developed through five main stages, from the Paleozoic to the early Mesozoic era. Stage 1; a shallow sedimentary basin was formed in the Oslo area leaving behind a succession called the Asker group, and this was left on top of deformed Cambro-Silurian sedimentary succession. This is dated between 315-324 Ma. Stage 2; the oldest volcanism left behind a layer of Basaltic lava, called B1, which is thickest in the Vestfold Graben and then thins northwards before it dies out around Oslo. This is dated between the late Carboniferous and early Permian. Stage 3; this is the main rifting stage, where Oslo Graben subsides and large quantities of rhomb porphyry, along with some basalt are released by crack eruptions in the ground. This dates between 298-292 Ma (Andersen et al., 2008). Stage 4; this is the main volcanism stage, where explosive volcanoes are formed and the period ends with caldera collapse. The sides of the rift are eroded, and form fan-shaped debris flow (Heeremans, 2005). This dates between 240-280 Ma. Stage 5; this is the final stage, large intrusions of syenitic to granitic composition, and small intrusions of Larvikite was placed in the Oslo Graben. This dates between 286-272 Ma. In all five steps there are dyke intrusions with a composition that is similar to basaltic lava (Andersen et al., 2008).

The continental crust in Oslo Graben have been influenced by rifting, melting, thickening and thinning. This variability in the continental crust's thickness makes it an interesting research (Heeremans, 2005). The thickness of the continental crust varies within the Oslo Graben and outside, but based on the Moho map in Stratford and Thybo (2009) the thickness of the continental crust in this area is estimated to be about 35 km. This thickness will therefore be used in the calculations in this thesis.

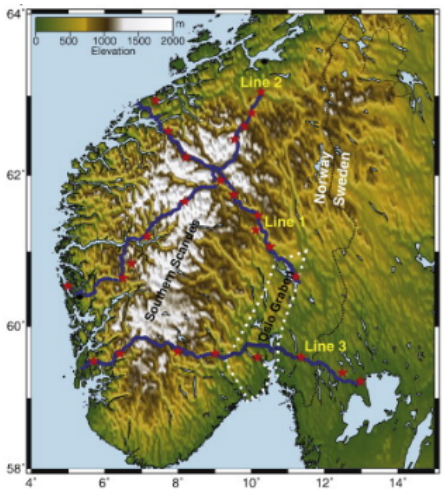

Figure 2: Magnus-Rex seismic experiment, Red stars(shot location) and blue dots(seismograph station). Profile line 3 i used in this section, and the forward modelling P-wave velocity is seen in figure 3 (Stratford and Thybo, 2011b).

The Fennoscandian continental crust beneath Norway has been mapped and studied for many decades (e.g. Ottemöller and Midzi (2003)). Stratford and Thybo found a new crustal thickness in the Oslo Graben that were 34 km +/- 2 km (Stratford et al., 2008). They found a 12 km lower crustal layer underneath the Oslo Graben that decreases into a 4 km lower crustal layer to the west and a 8 km lower crustal layer to the east, see figure 3. There is also observed strong reflectors in the mantle underneath the Oslo Graben, which indicate that the deformation goes further down into the mantle layer. Sub-horizontal mantle reflectors are common in the Oslo Graben and the Fennoscandian shield (Tryti and Sellevoll (1977): Stratford et al. (2009): Stratford and Thybo (2011a): Stratford and Thybo (2011b)).

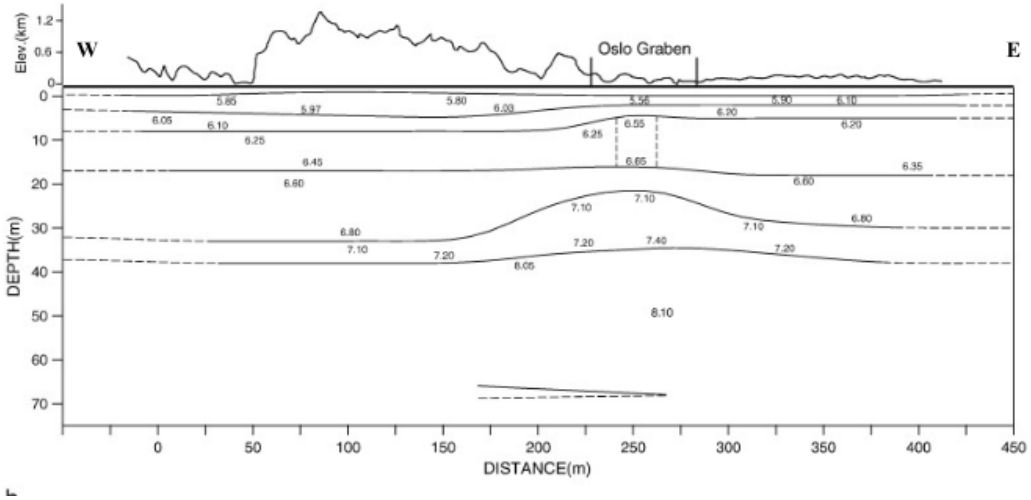

Figure 3: Forward modelling P-wave velocity solution for line 3 in 2. Notice the lower crustal layer, and the mantle reflector marked at 65 km depth as a dashed horizontal line and dipping line. Numbers are the P-wave velocity(km/s) (Stratford and Thybo, 2011a).

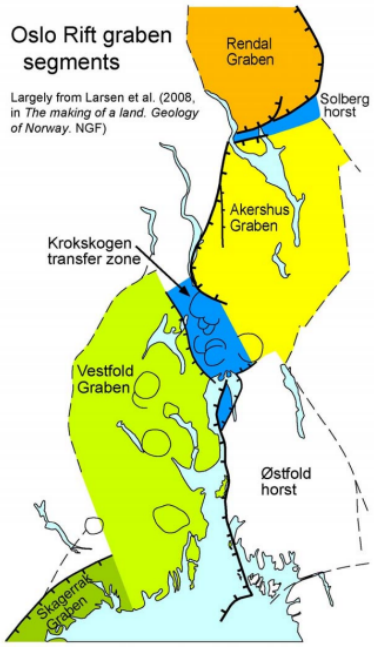

(a) Map of the different segments in the Oslorift. Oslo Graben consists of Akershus Graben, Vestfold Graben and Krokskogen tranfer zone in between them (Andersen et al., 2008)

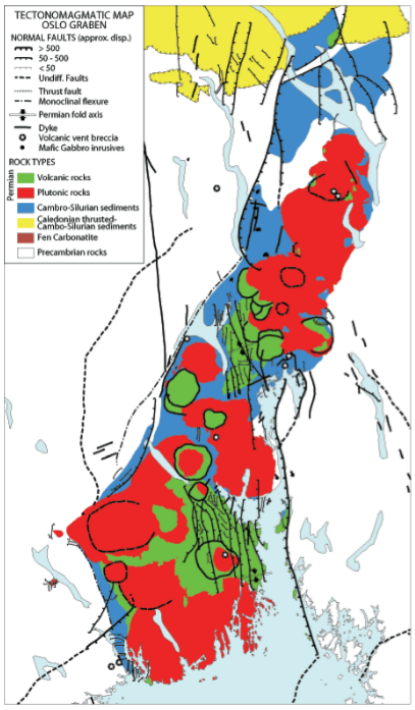

(b) Tectonomagmatic map of Oslo Graben (Heeremans, 2005).

Figure 4: Geological maps of the Oslo Graben

Figure 1 shows that KONO1, KONO4, KONO5 and KONO6 lies within the Oslo Graben, where KONO1, KONO5 and KONO6 lies in Vestfold Graben, and KONO4 lies in the Krokskogen transfer zone in a area affected by thrust faults. KONO5 and KONO6 lies near the Oslofjord, where the area surrounding KONO5 is heavily influenced by thrust faults.

Outside of the Oslo Graben on Archean and Proterozoic basement, the stations KONO, KONO2, KONO3, KONO7 and KONO8 are located. The permanent station KONO is located outside of the surface expression of the Oslo Graben, but the station lies above a middle and lower crust that is heavily affected by the rifting during the formation of Oslo Graben (Kolstrup and Maupin, 2013). KONO2 and KONO3 also lies in close proximity to the border, and may be located in a similar geological setting as KONO. KONO2 and KONO3 does however lie close to a long stretching fault (Heeremans, 2005).

3 Interfaces in the Earth and wave propagation

3.1 The crust and mantle in the Earth

The Earth consists of primarily three parts, which is the crust, mantle and core. The mantle is about 2890 km thick, and consists dominantly of olivine in the top 500 km and spinel in the lower 2000 km. While the mantle between 500 and about 900 km is most likely a gradual transition between the two (Meinesz, 2012).

Based on seismic refraction data, a researcher named Mohorovicic identified in 1909 through their arrivals, two P-waves. One travelled through a deep high velocity layer, while the other direct P-wave travelled through a more shallow layer with a slower velocity. These two layers were the crust and mantle, and the boundary between them was named Moho after Mohorovicic. The Moho is between 0-5 km thick and may be a sharp or a complicated transition zone depending on their location (Stein and Wysession, 2009).

There are two types of crusts, the oceanic crust which is about 7 km thick, and the continental crust which is thicker and varies (Stein and Wysession, 2009). The crust around the Kongsberg area is between 34-40 km thick (Stratford and Thybo, 2009). In this thesis it is set to 35 km, when we need a value to make calculations. The focus will be on the continental crust and the mantle, and what happens when the incident P-wave hits Moho, and converts or reflects of the boundary.

3.2 Incident P-wave and multiples

Seismology is the study of elastic waves that travel through the Earth. These waves originate at a source that either occurs naturally, like earthquakes, or artificially by controlled explosions. The two main waves are the P-wave (also called pressure or primary wave), and the S-wave (also called shear or secondary wave). The P-wave is the fastest, and a compression wave that has particle motion in the same direction as the propagation. While the S-wave is a shear wave and has particle motion perpendicular to the wave propagation. The S-wave is further divided into two components, called SV and SH. The SV is shear waves with displacement in the vertical direction, while SH is shear waves with displacement in the horizontal direction (Stein and Wysession, 2009).

Seismic waves are sensitive to sudden variations in acoustic impedance (velocity multi-

plied with density). In the ground these variations happen when the waves travel through a horizontal discontinuity or boundary between layers. The incident P-wave is analysed more because this wave arrives first and is thereby least likely to be influenced by other primary phases. The incident P-wave will split into four waves with different energy when it hits a discontinuity, which can be calculated using Zoeppritz equations (Rondenay, 2009). When the incident P-wave meets the boundary Moho it generates a reflected and transmitted P-wave, but part of the P-wave is converted to a reflected and transmitted SV-wave, as seen in figure 5a. If the incident wave is a SV- wave, there will also be generated reflected and transmitted P- and SV- waves, while the incident SH- wave only generates a reflected and a transmitted SH- wave (Stein and Wysession, 2009).

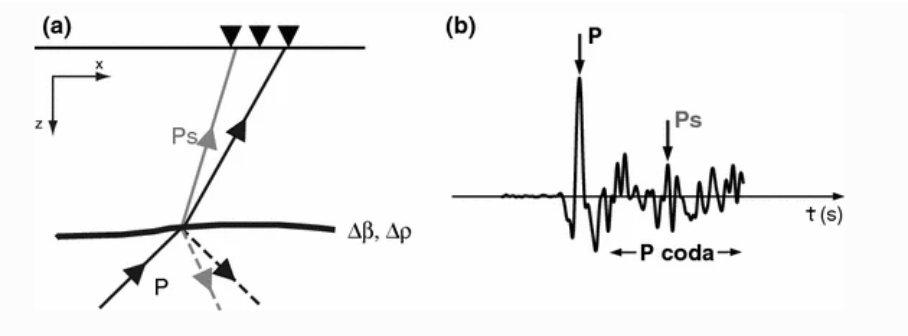

Figure 5: In a) One can see the incident P-wave at a discontinuity, and the transmitted and reflected waves generated at this boundary. b) Shows an example of a seismogram, and the arrival of the P- and Ps-wave. The delay time between the P- and the Ps-wave helps to find the thickness of the upper layer. (Rondenay, 2009)

Figure 5b shows an example of a seismogram, and the arrival of the P- and Ps-wave. The delay time between the P- and Ps-wave is used to find the thickness of the upper layer. In this thesis the interface considered is the Moho boundary, so the upper layer is therefore the continental crust. When the incident wave hits this boundary, the four waves will have a energy between 0 and 100 percent of the incoming energy, and together they are equal to a hundred percent because of the conservation of energy. In the cases where the velocity and density of the two layers are similar, most of the energy will go to the transmitted wave that is of the same wave type as the incident wave. Therefore, the converted S-wave will be small (Stein and Wysession, 2009).

The crust and mantle is a solid-solid interface, and thereby the displacement and

traction are continuous. For this to be the case at the interface for all distances and times, the horizontal wavenumber along the interface have to be the same for all waves. This causes the waves to have the same apparent velocity along the interface and stay in phase. If this is fulfilled, then equation 1, also called Snell's law, can be used to find the incident angles of the transmitted and reflected waves at Moho by using the incident angle of the incoming wave (Stein and Wysession, 2009). The angles are measured between the rays, and the normal to the boundary between the two layers (Mussett and Khan, 2000).

$$\frac{sini_1}{v_1} = \frac{sini_2}{v2} \tag{1}$$

Here, the i_1 and v_1 are the incident angle and velocity, while the i_2 and v_2 are the angle and velocity of the converted wave (Mussett and Khan, 2000).

In addition to the P- and Ps- wave, the incident P-wave also generated waves that are later reflected multiple times between the surface and Moho and that may have been converted to S-waves before arriving at the station, and these are called multiples or multipathing. In figure 6b, three different multiples and their names are listed. Their names are given by their wave path and whether the wave transmitted, reflected or converted to a P- or S- wave upon hitting the interface (Bath and Stefánsson (1966): Mussett and Khan (2000)).

There is also something called scattering of seismic waves, and the difference with conversion is gradual (Stein and Wysession, 2009). This is caused by heterogeneities in the Earth, and causes the wave amplitude to be reduced (Herraiz and Espinosa, 1987). Scattering is important in the continental crust, because this layer may contain many small layers, dipping layers and reflectors. The scattered energy also forms a tail after the arrivals which is called a coda, and this is discontinued energy that dissipates after a certain time. The scattered energy comes from all directions, and thereby does not show any or little preferred particle motion, which is in contrast to the main arrivals (Stein and Wysession, 2009).

The radial component in figure 6a shows the arrivals of the converted P- to SV-waves, while the vertical component shows the transmitted, reflected and converted waves, but the converted waves are smaller. The direct P-wave in the vertical component has a

more prominent peak, but the radial component still shows a clear arrival of the direct P-wave (Stein and Wysession, 2009). There is however a visible PPmP- wave at the radial component that is about 1/3 of the size as the one in the vertical component. This wave is a result of; an incident P-wave that is transmitted on the Moho boundary into a P-wave, then reflected on the surface to a P-wave, and again at the Moho, until it arrives at the receiver. If the Moho boundary is plane layered and the incident waves have small angles, then this wave will be removed when the radial component is deconvolved (see section 5.4) (Langston, 1979).

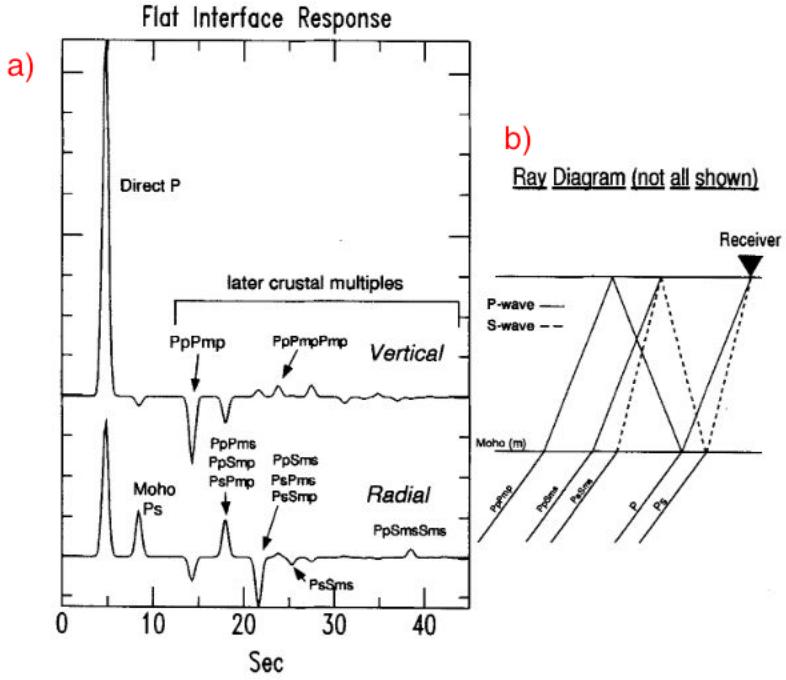

Figure 6: Arrivals expected from interaction of a P- wave and the Moho. a) shows the direct P-wave and the expected time of arrival for the multiples after the direct P-wave, on the vertical and radial component. While, b) shows the travel paths that the different waves have taken, and their names accordingly (Clouser and Langston, 1995).

When the boundary layer is dipping, the reflection phases become more complicated and if the angle is steep the stacking of events gives a seismogram that is not correct in relation to it's geometric position. The dipping layer is taken into account when the seismic events are put through the migration process, which restores their geometric situation (Reynolds, 2011).

4 Data collection and processing

This section starts with presenting the information about the permanent station KONO and the eight temporary stations. Followed by the collection of data. Next, the three different steps; removing the instrument response, partitioning of the signal and deconvolution are explained, which results in P-receiver functions. Finally, stacking of events to improve signal-to-noise ratio, and conversion and reflection points at each of the nine stations are presented.

4.1 Seismic stations

The seismometer station KONO is located in an abandoned silver mine, consisting of Pre-Cambrian gneiss. The mine lies 340 meters below the surface, and 2200 meters into the side of a hill (see figure 7). The seismometer is placed on concrete floor that lies on top of bedrock, and the temperature and humidity are consistent. KONO has been active since 1 September 1978 (U S Geological Survey(USGS), accessed: 7. June 2020). Eight temporary stations were placed within a 50 km radius around KONO, and the project started on the 6th of April 2018 and lasted until April 2020. The temporary stations are called KONO1- KONO8, and their position in comparison to KONO can be seen in figure 1. Information on the stations has been provided by Annie Jerkins (Personal communication, 1 April).

Figure 7: The seismometer placed at KONO

KONO1 is placed in Mjøndalen, and the seismometer is located in the garage of a house that lies at the end of a street. The seismometer is placed on bedrock. There is a horse stable about 300 meters down the street, but little traffic and noise in the

area around the house. KONO2 is placed in Breidsethytta, located in the garage of an old DNT cabin. This is a quiet area, with no other houses or cabins nearby. The seismometer is placed on bedrock. KONO3 is placed in Blefjell, and is located in the basement of Ble sportskapell, on bedrock. This is also a quiet area with no people in close proximity. KONO4 is placed in Lommedalen, and is located in the basement of a large cabin, on bedrock. This is a calm area. KONO5 is placed in Horten, and is located in the basement of a house. From NGU'S map we can see that the area consists of marine and fjord deposits, so this seismometer may not be placed directly on bedrock (Norges geologiske undersøkelse(NGU), accessed: 10.06.2020). There is however a water pipe at this location that may cause some noise in the data. KONO6 is placed in Sandefjord, and is located in the shed of a house. From NGU's map it looks like the seismometer is placed on bedrock or ocean deposits (Norges geologiske undersøkelse(NGU), accessed: 10.06.2020). At this location there can be some noise from traffic. KONO7 is placed in Kveiteseid, and is located in a garage by a farm. The seismometer is located in an area with moraine deposits (Norges geologiske undersøkelse(NGU), accessed: 10.06.2020). The instrument is placed in a building with goats, and the garage is sometimes used as a carpenter workshop, and this causes the data to have a lot of noise. KONO8 is placed in Vegglifjell, and is located in a potato cellar in a house at the end of a street. The seismometer is placed directly on bedrock, and there is no traffic or other human made noise in the nearby area. From NGU's map we can see that the area consists of bedrock and moraine deposits (A. Jerkins 2020, personal communication, 1 April).

4.2 Collection of data

In this thesis, the seismological data recorded at the eight temporary stations KONO1-KONO8, and the data from the permanent station KONO are used. The data was collected between April 2018 and September 2019. Both the temporary and permanent stations are three component seismographs. The three components are measured in the North-South(N-S), East-West(E-W) and vertical(Z) direction.

The data from the permanent station KONO was collected from the IRIS website. The seismic waves travel long distances before arriving at the stations, and thereby one needs earthquakes with a strong amplitude to get clear arrivals. This is why earthquakes

with a magnitude of 5.5 or higher were selected (Frassetto and Thybo, 2013). The time window for the events was set from the time when the eight temporary stations were put out in April 2018, and up to the date they were collected in September 2019. Within this period, 672 events were identified and the list was downloaded from the IRIS website.

The list of events was loaded into MATLAB, to find the events within a great-circle-path distance of 30-95 degrees from KONO with the help of their latitude and longitude. 219 events are located within this range and these are put in a document with their date, time, latitude, longitude and depth. The range was first set to 25-95 degrees, but only two events were located in the 25-30 degree field. The lower value was changed from 25 to 30 degrees because when the epicentral distance is larger than 30 degrees we avoid triplicated P-waves from the mantle transition zone (Rondenay, 2009). The raw data from KONO was then converted into SAC files.

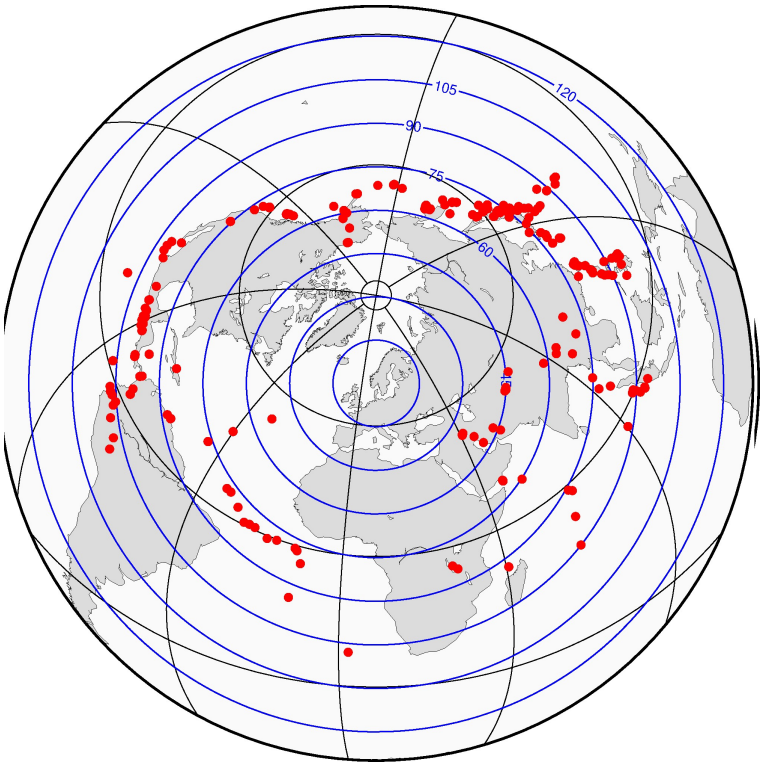

Figure 8: Map of seismic events between 30-95 degrees from KONO, in the period April 2018 to September 2019.

The map in figure 8 shows that most of the events are located along the Japanese coast and along the west coast of America. These two coasts are part of an area called "Pacific

Ring of Fire", where the majority of the world's seismic activity originates (National Geographic Society, accessed: 11. Mai 2020). Some events originate from the Atlantic Ocean, and these are located in close proximity of the Mid- Atlantic Ridge.

The seismic data from the eight temporary stations was collected with the help of NORSAR. A list of 219 events was sent with a data request for the given days, and this was received in mSEED format. In addition, eight files that contained the stations transfer functions was received, for each of the eight stations, in seed format. The eight seed files had to be run through the RDSEED program, and the output was the RESP files for the three different components, for each of the eight stations (Goldstein and Snoke (2005): Helffrich et al. (2013)). Then the raw data from KONO1-KONO8 was converted into SAC files for further processing.

4.3 SAC-Seismic analysis code

SAC stands for "Seismic Analysis Code", and was developed in the 1980s. SAC was created to help seismologists with the study of seismic events, and can be used for both quick analysis and more detailed research. SAC is a interactive program that is designed to study intervals of signals. It is especially well-suited for time-series data, which makes it a good program to use when processing the data in this master thesis (Goldstein and Snoke (2005): Helffrich et al. (2013)). The files from the different events for KONO and the temporary stations are converted into SAC files by using the program mseed2sac. This converts the mSEED files to SAC format.

Figure 9 shows the raw data from a event located Northwest of Kuril Islands, in the N-S, E-W and vertical direction. Plot BH1 represents the N-S, BH2 the E-W and BHZ the vertical direction. The signal shows a clear increase around 600s on BH1 and BHZ, and according to iasp91 this is the arrival of the direct P-wave. Shortly before 1100s, there is a clear peak on BH1 and BH2, and this is the arrival of the direct S-wave (Kennett, 1991). Band-pass filters were tested on the data, with varying corner frequencies between 0.02 to 4.0 Hz. This made it possible to get a more clear plot without some of the noise, and to get an indication as to what filter should be applied later (Frassetto and Thybo, 2013).

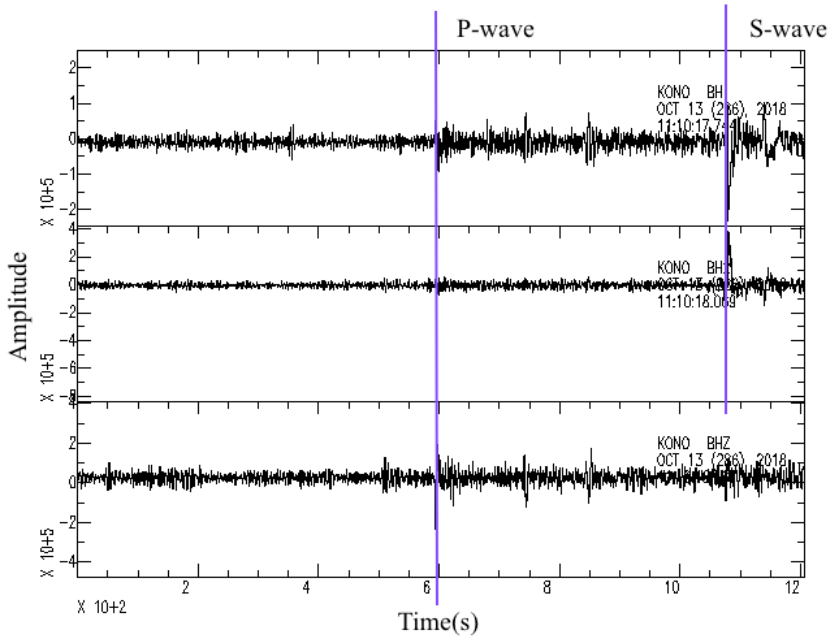

Figure 9: Raw data from the three components plotted in SAC, where the top one is BH1, the middle is BH2 and the bottom one is BHZ. This event is from the Northwest of Kuril Islands with a magnitude of 6.7, and depth 461 km, measured at KONO.

4.3.1 Time interval cutting

The data from the eight temporary stations was cut using a bash script. The signals retrieved from these stations covered the whole day, and this had to be cut to the time interval of the given event. This was done by reading the depth, date, time and the latitude and longitude for the seismic station and the event, into a SAC macro file. The list of events were loaded into SAC macro, and the origin time of the event was changed to this reference time. Then the command >traveltime picks 0 phase P was used, which calculates the travel time for phase P from iasp91 or ak135 (Goldstein and Snoke, 2005). The signal was then cut five second before the expected arrival for the direct P-wave, and thirty seconds after its arrival. This time window was chosen to get a clear plot of the arriving direct P-wave and the crustal multiples that is formed at Moho, see figure 6 (Goldstein and Snoke, 2005).

4.4 Removing the instrument response

Three RESP files from the permanent station KONO were collected from the IRIS KONO seismic station website, and these contained the instrument response to the three channels BH1, BH2 and BHZ. While the RESP files for the eight temporary stations KONO1-8 were collected from NORSAR, containing the instrument response to the three channels HHE, HHN and HHZ.

The SAC script first removes the linear trend and mean from the data, and then uses the command "transfer". This command deconvolves the data by removing the instrument response that is stored in the RESP files, and converts it to displacement. It is recommended that frequency limits are applied to the signal when the data is converted to displacement. Four limits are applied, where two are high-pass filters at low frequencies and the last two are low-pass filters at high frequencies. It is important when choosing the different frequencies that it is not too narrow. The general condition is; f1 <f2 <f3 <f4 (Goldstein and Snoke, 2005). In the data used in this thesis, the limits chosen are 0.002, 0.004, 3.0 and 5.0. The first two limits remove all periods lower than 500s from the results, and are then smoothly increased to one by 250s period. The high frequencies can be nearly as high as the Nyquist frequency: 0.5/sampling interval, but they should be less (Goldstein and Snoke (2005): (Ammon, 2015)). The temporary stations have a sampling interval of 0.01, and the high frequencies can then be about 50 Hz at most. But to get results within a interesting seismic passband, the f4 is set to 5.0 Hz (van der Lee, 15. August, 2011).

In Figure 10 the ground displacement from the earthquake is displayed after instrument deconvolution. The data shows less noise in the signal, and the direct P- and S-wave at 600s and 1100s are more prominent. The signal has improved, and can observe that the low frequencies are more stable, but there are still microseismic noise present in the beginning of the plot, before the arrival of the direct P-wave at 600s (Ammon, 2015).

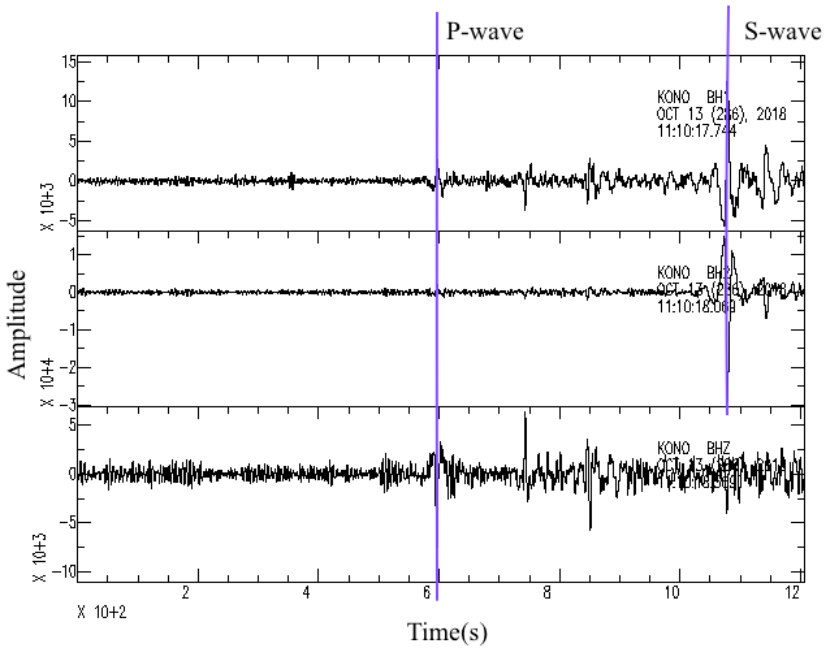

Figure 10: The data from figure 9 after it is deconvolved to displacement.

4.5 Partitioning of the signal

In order to isolate and separate the incident and scattered wave fields, the three components are rotated from North-South(N-S), East-West(E-W) and vertical(Z), to Radial(R), Transverse(T) and Vertical(Z) components. This rotation relies on the assumption that the incident P-wave is almost vertical, which thereby leads to the incident wave field being only visible in the vertical component, while the converted waves are confined to the radial component. In this thesis the incident wave is however between 10-30 degrees, and thereby the incident and converted wave fields are visible on both the radial and vertical component (Rondenay, 2009). This is because when the signal is partitioned into the R, T and Z component, the energy of the P- and SV- wave is split into the radial and vertical component. While the SH- wave is only visible on the transverse component (Stein and Wysession, 2009).

Figure 11a, shows how the N-S and E-W direction lie in comparison to the rotated radial and transverse components. The transverse lie 90 degrees from the radial, while

the vertical component remains unchanged. This is however the first of three possible rotations. To isolate the incident and converted wave fields to separate components, the data can be further rotated to the L, Q, T components or to P, SV and SH components. The data is however not rotated further to these two components because I am not only interested in the Ps- wave, but also a later arrival that may not be an SV- wave, but a PPmP. The quality of the direct P-wave is also central, because this arrival is used as a reference point in relation to later arrivals and noise. This arrival disappears in the Q component when the data is rotated to L, Q and T components. All three rotations separate the waves based on the assumption that the boundaries are plane, horizontal and isotopic (Rondenay, 2009).

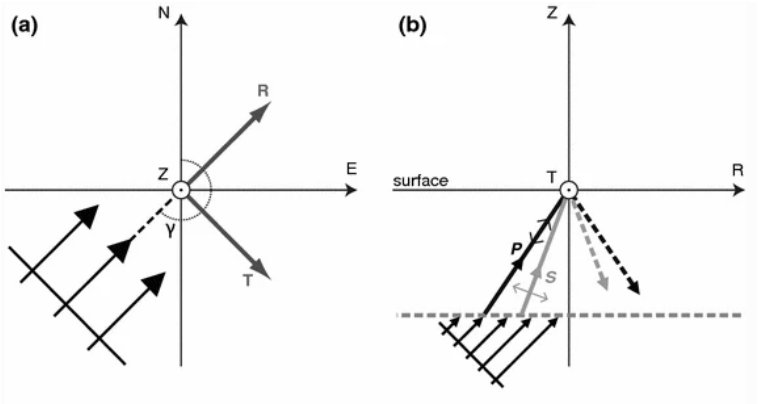

Figure 11: a) Projection axis for imaging purpose. Rotation from N-S, E-W and Vertical directions, to Radial, Transverse and vertical components. The angle γ is the back azimuth of the incident wave (Rondenay, 2009). b) The vertical profile of the longitudinal plane, where the incident wave hits the Moho marked by the dashed horizontal line. The upgoing solid lines for the P- and S- wave and their free-surface reflected waves marked by dashed lines. The propagating direction is marked by the closed arrow, while the polarization of the waves are marked by open arrows (Rondenay, 2009)

A bash script was used to rotate the data, and this had to be split into two steps. The first one defined and found the missing parameters in the SAC header for each of the events. This included date, time, latitude, longitude, depth of the event, and the azimuth and back azimuth component. In addition to this, the latitude and longitude for the nine separate stations are set.

The second script rotates the events coordinate system from N-S, E-W and vertical direction, to R, T and Z components. This was done by using the command >rotate to

gcp, where gcp stands for great circle path. Equation 2 gives the formula for this rotation (Rondenay, 2009).

$$\begin{pmatrix} R \\ T \\ Z \end{pmatrix} = \begin{pmatrix} -cos\gamma & -sin\gamma & 0 \\ sin\gamma & -cos\gamma & 0 \\ 0 & 0 & 1 \end{pmatrix} \begin{pmatrix} N \\ E \\ Z \end{pmatrix} \tag{2}$$

The N, E and Z are the N-S, E-W and vertical direction, while the R, T, Z are the components that the signal is rotated into. Gamma(γ) is the back azimuth of the incident ray (Rondenay, 2009).

Figure 12 shows the rotated and cut section for the event shown in figure 10. The predicted arrival time of the incident P-wave is marked with a line. This is done by using the command >traveltime picks 0 phase P. The command sets the origin time for when the earthquake happens, calculates the travel time for phase P from iasp91 and a line is drawn as to when it is expected to arrive. This time estimate is accurate for most of the events, but some events have a direct P-wave arriving some seconds before or after it's expected arrival time (Goldstein and Snoke, 2005). In this case we see that the direct P-wave arrives about 2s later than the marked line. The P-wave is visible only on the radial(R) and vertical(Z) component, which have a higher amplitude than the transverse(T) component. This fits well with the theory and presumed assumptions.

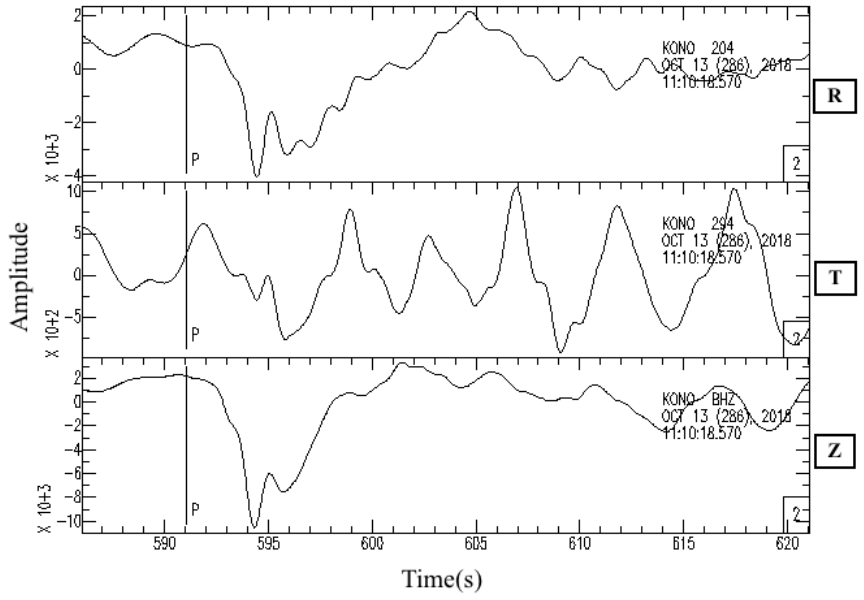

Figure 12: Partitioning of the signal into Radial (top plot), Transverse (middle plot) and vertical (bottom plot) components.

4.6 Deconvolution

In order to reduce the noise, the data is first filtered using a 2nd order Butterworth band-pass filter, with passband 0.05-3.0 Hz (Frassetto and Thybo, 2013). This is a zero-phase filter which means that after the signals are filtered in the forward direction, the filtered data is then reversed back through the filter. The receiver functions from South America show more noise, most likely caused by Rayleigh waves from the ambient noise in the Atlantic Ocean. The data is therefore filtered using two filter ranges, one from 0.05-0.16 Hz and the other between 0.8-3.0 Hz, to avoid the noise range between 0.16-0.8 Hz (Douglas, 1997).

The final step is to deconvolve the data. The purpose of deconvolution is to separate the Earth's seismic impedance(velocity and density) contrast, from the influence of the source- and instrument impulse response (Sawade, 2018). If this step is successful, the arrival of the direct P-wave and other converted phases at Moho, will become sharpened

(Rondenay, 2009). In this thesis the direct and converted waves are generated from an upgoing P-wave that is propagating through the structure in the ground beneath the seismic station (Frassetto and Thybo, 2013). The different steps to deconvolve the data are listed below, and a scrip in MATLAB by Stéphane Rondenay is applied. The focus will be on the radial component, since this is the receiver functions that will be used in this thesis.

When the incident P-wave travels through a plane or dipping interface, as for example Moho, it causes a theoretical displacement response. The equations are in the time domain, and are expressed for each of the three components in equation 3, 4 and 5 (Langston, 1979).

$$D_Z(t) = S(t) * I(t) * E_Z(t) \tag{3}$$

$$D_R(t) = S(t) * I(t) * E_R(t) \tag{4}$$

$$D_T(t) = S(t) * I(t) * E_T(t) \tag{5}$$

In equation 3, 4 and 5, the * stands for the convolution operator. The D(t) is the recorded signal in the R, T and Z direction, S(t) is the source time function of the impinging wave, I(t) is the instrument impulse response and E(t) is the structure impulse response to each of the three components (Langston (1979): Sawade (2018)). In this thesis, the instrument response, I(t), has been removed (see section 4.1), so the I(t) is omitted. The data now has to be transformed from the time- to the frequency domain, and this is done by computing the discrete Fourier transform(DTF) using the fast Fourier transform(FFT) algorithm. The convolution *, now becomes multiplication, and are now left with equation 6, 7 and 8 (Stein and Wysession, 2009).

$$D_Z(w) = S(w)E_Z(w) \tag{6}$$

$$D_R(w) = S(w)E_R(w) \tag{7}$$

$$D_T(w) = S(w)E_T(w) \tag{8}$$

In equation 6, 7 and 8, the w represents the frequency. The radial receiver function is by definition the impulse response on the radial component relative to the impulse

response on the vertical component, as seen in equation 9 (Ammon, 1991).

$$r(w) = \frac{E_R(w)}{E_Z(w)} = \frac{D_R(w)}{D_Z(w)} \tag{9}$$

Where the r(w) in equation 9 represents the radial component. This equation is however numerically unstable because when the denominator approaches zero, the noise will become amplified. This can be stabilized by regularising the vertical component, by multiplying the vertical signal D_Z with a complex conjugate in both the nominator and denominator, and adding a water level to the denominator (Rondenay, 2009). The water level is introduced to avoid division by zero or small values, when $D_Z(w)D_Z^*(w)$ becomes small (Gurrola et al., 1995).

$$r(w) = \frac{D_R(w)D_Z^*(w)}{D_Z(w)D_Z^*(w) + \epsilon} \tag{10}$$

$$t(w) = \frac{D_T(w)D_Z^*(w)}{D_Z(w)D_Z^*(w) + \epsilon} \tag{11}$$

$$z(w) = \frac{D_Z(w)D_Z^*(w)}{D_Z(w)D_Z^*(w) + \epsilon} \tag{12}$$

Equation 10, 11 and 12 show the stabilised equations. Where the * represents the complex conjugated, ϵ represents the water level and t(w) and z(w) represent the transverse and vertical component.

The water level should be set, so that the noise will not be blown up. Normally, the transverse component should not show P- and SV- waves, and its amplitude can be used to evaluate the noise level and fix the water level, as seen in equation 13. In this thesis the water level is calculated using a dampening factor of 0.25, which is termed water in equation 13. Different dampening factor between 0.1-0.5 were tried, but I found that 0.25 gave good results (Clayton and Wiggins, 1976).

$$\epsilon = water * max|D_T(w)D_T^*(w)| \tag{13}$$

In equation 13, water is the dampening factor, while $D_T(w)$ is the transverse signal, and $D_T^*(w)$ is the conjugated transverse signal.

After the deconvolution, the $r(w)$ is transformed back to the time domain r(t), by computing the inverse discrete Fourier transform using the inverse fast Fourier transform algorithm. This is applied to find the radial receiver function, r(t), that will be used in this thesis, but the transverse, t(t), and vertical, z(t), receiver function can be found through the same method as seen in equation 11 and 12 (Stein and Wysession, 2009). The transverse receiver function shows the reflected and transmitted SH-waves, and if this is nonzero, it is an indication of anisotropy, scattering or a dipping layer (Savage, 1998).

In figure 13 the vertical receiver function shows a clear arrival of the P-wave coming in at 5s, but the rest of the signal shows low frequency noise. The radial receiver function also show the arrival of the direct P-wave, but the arriving multiples after this are more prominent. There are positive peaks between 5-10s, a clear negative peak at about 15s followed by a positive peak at 20s. The transverse receiver function shows no clear arrivals, but the signal consists of low frequency noise approaching zero. This is used when finding the water level for each receiver function. The radial component is called the receiver function(RF) in this thesis.

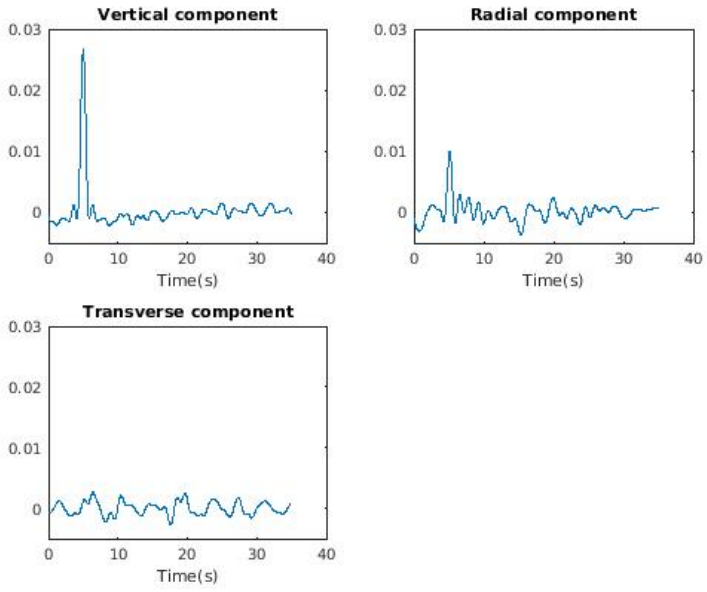

Figure 13: The data from figure 12 in the Radial, Transverse and vertical component after deconvolution. The radial component is called receiver function.

The x-axis in figure 13 and 14 show 5s before the direct P-wave arrival, and 30s after.

The three different components are further divided by the maximum value of the vertical component, so the radial and transverse component becomes normalised to the vertical, see figure 14. This does not change the results, but is important when stacking the events, because all the events will then have the same max direct P-wave amplitude.

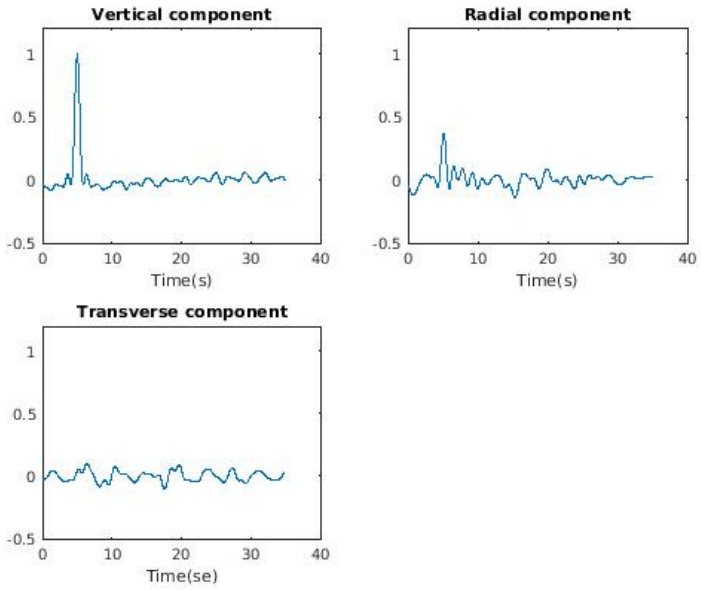

Figure 14: The data from figure 13 after the three components have been normalized with the maximum value of the vertical component.

4.7 Stacking of Receiver functions

When using teleseismic earthquakes, it is important to consider the reduction in amplitude that the reflected and transmitted waves go through at interfaces. The reduction of wave amplitude can originate from geometric spreading, scattering, multipathing and anelastisity (also called intrinsic attenuation). In the first three the energy in conserved in the propagating wave field, but in the last one the energy converts into heat and the energy is therefore lost (Stein and Wysession (2009): Sawade (2018)). By stacking the events, the signal-to-noise ratio (SNR) is improved and the seismic phases becomes sharpened (Rondenay, 2009).

In this thesis, the data is stacked by clusters, and the back azimuth value vary within 30-40 degrees of each other. I utilize four cluster areas, as seen in figure 8, that have

multiple events which lie in close proximity to each other. These clusters are located in the Japan region, with a back azimuth value between 15-52 degrees, in the Philippines and Indonesia region, with a back azimuth value between 58-93 degrees, on the west coast of Alaska and Canada with a back azimuth value between 332-6 degrees, and on the west coast of South America with a back azimuth value between 269-305 degrees (Cassidy, 1992). The radial component for each event are saved, and stacked by adding all short period events from the same area, and then dividing by number of events. The receiver functions from South America that consist of two frequency ranges are first added together, before they are stacked in the same way. 150 seismic events produced acceptable receiver functions in these four cluster areas, and was used in the stacking of RFs.

When stacking the signals, some events are too noisy, and these are removed before stacking. The envelope of the signal is calculated using the Hilbert Transform (Mathworks, R2020a). The maximum value of the envelope is divided by the average value, and if this number is lower than the set number 2.5, the signal is too flat and the receiver function is removed. The number was first set to 3.0, but this eliminated signals that showed a clear direct P-wave arrival in the receiver function, so this was changed to 2.5. When these signals were removed, the stacked receiver functions gave higher and more clear arrivals, because the signals that contributed to the flattening of the stacked RFs was removed.

The receiver functions show two types of wave periods, where one is long and the other is short, as seen in figure 15. In figure 15 the RFs marked in red are the long periods and the RFs marked in black shows the short. These two period ranges are separated, and then the short periods are further used in the stacking of RFs. This is because these RFs give sharp direct P-wave arrivals at 0s, and the signals are not equally affected by noise.

The longer periods(marked in red) in figure 15 show a lot of noise, and the arrival of the direct P-wave are shifted either 1-2s before or after 0s. This can be caused by the noise in the signal, which limits the effect of the deconvolution. While the shorter periods(marked in black) show a clear arriving direct P-wave at 0s, and a negative peak around 10s. Therefore the longer period traces are removed, so that the stacked RFs give a good representation of the direct and multiple waves.

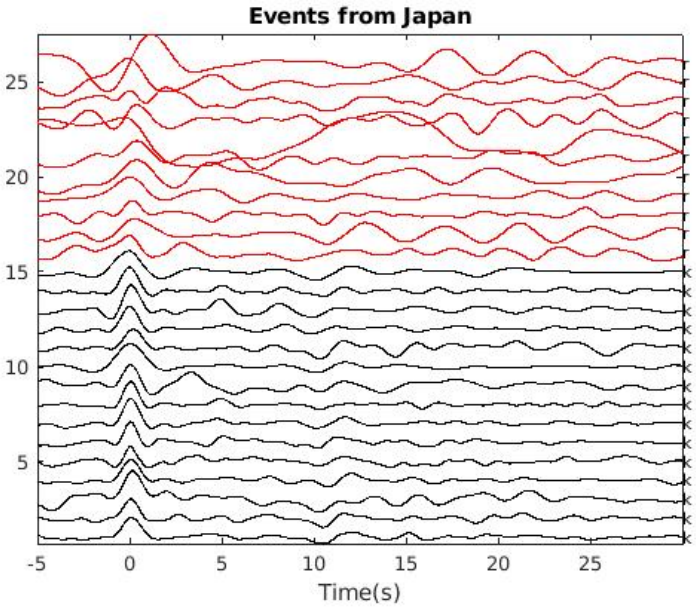

Figure 15: Events from the Japan area, measured at KONO1. Short periods are marked in black, and long periods are marked in red.

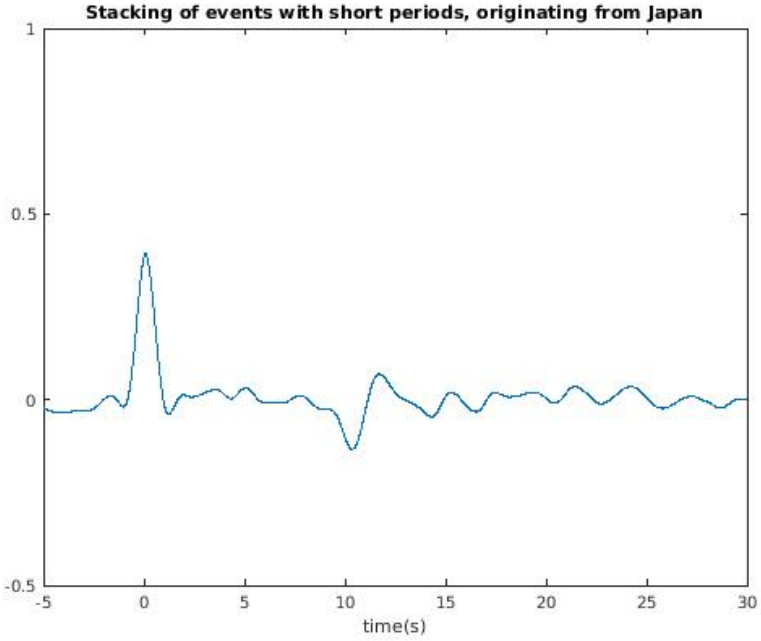

Figure 16: The short period events from the Japan area in figure 15 are here stacked. Measured at KONO1.

Figure 16 shows the stacked RF of the short period events in figure 15.

4.7.1 P-Ps time-difference

Usually when stacking events, corrections are made for each event for the different incident angle for all the incident waves. In this case the longest and the shortest distance to KONO are found, and the delay time between the arrival of the P- and Ps- wave converted at Moho are calculated (Frassetto and Thybo, 2013). The delay time to the maximum and minimum distance for each of the four areas are calculated.

The thickness and velocity of the crust and mantle used in this calculation is based on the refraction experiment found in Stratford and Thybo (2009). From this, the thickness of the first layer is about 35 km(h), the P-wave velocity in the crust is 6.8 km/s(α_1), the P-wave velocity in the mantle is 8.1 km/s(α_2), the S-wave velocity in the crust is 3.9 km/s(β_1) and the S-wave velocity in the mantle is 4.5 km/s(β_2). The slowness value for the different max and min events are found in the book IASPEI91 (Kennett, 1991), where the P-wave slowness value is used. Start by finding the incident angle in the mantle, which is found through equation 14.

$$i = arcsin(slowness * \alpha_2) \tag{14}$$

This incident P-wave angle in the mantle is then used to calculate the incident angles for the P-wave and Ps-wave in the crust, separately. This is done by using Snell's law (see section 3.2), as seen in equation 15.

$$\frac{sini}{\alpha_2} = \frac{sini_p}{\alpha_1} = \frac{sini_s}{\beta_1} \tag{15}$$

Equation 15 employs the incident angle and velocity of the P-wave in the mantle, and the velocity of the P-wave and S-wave in the crust, to find the angle of the transmitted P- and Ps-wave. In these calculations the angle for the P-wave is larger than for the Ps-wave. The crustal travel time can now be calculated using equation 16.

$$t_p/t_s = \frac{h}{cos(i_p/i_s)} * \frac{1}{\alpha_1/\beta_1} \tag{16}$$

Because the Ps-wave uses additional time in the mantle in comparison to the P-wave,

this has to be calculated and added to the travel time for the Ps-wave before finding the time difference. This additional time is calculated using equation 17. Where the d is found through equation 18.

$$t = \frac{d * sin(i)}{\alpha_2} \tag{17}$$

$$d = h(tan(i_p) - tan(i_s)) \tag{18}$$

In table 1 the delay time between the P- and Ps-wave for the events that have the max and min distance to the receiver are calculated for each of the four areas. The difference in delay time between the two distances are also listed in the final column.

Location	Max/Min distance(km)	Delay time	Delay time difference
Japan	Max	3.93s	0.10s
	Min	4.03s	
Philippines and Indonesia	Max	3.91s	0.12s
	Min	4.03s	
Alaska and Canada	Max	4.00s	0.10s
	Min	4.10s	
South America	Max	3.91s	0.09s
	Min	4.00s	

Table 1: Delay time between the P- and Ps-wave, for each of the four areas.

Table 1 shows that there are little differences in the delay times between the arriving P- and Ps-wave. The difference is less than a second, despite that the incident angle for each of the events vary between 19 and 29 degrees. Therefore it is unnecessary to put the data through moveout corrections, because the delay time between the two waves are much smaller than the dominant period (Rondenay, 2009).

4.8 Conversion and reflection points

The Ps- and PPmP- waves to the different events, can be traced back to where they have their conversion or reflection point at the Moho (Makushkina et al., 2019). This is

used when doing migration and the points that overlap can be stacked, regardless of the station. In this thesis I do not migrate, but use the points to compare where conversion or reflection has occurred at the nine stations. The conversion does not occur only at one point, but in a zone called the Fresnel zone (Stein and Wysession, 2009).

The location of where the Ps- waves transmit at Moho is found by using the S-wave velocity, while the P-wave is used when finding the reflection point of the PPmP- waves. The slowness value of the direct P-wave is found through Kennett (1991), and are then used in the formula expressed in equation 19.

$$X = \frac{p * h}{\sqrt{1/(\alpha_1 or \beta_1)^2 - p^2}} \tag{19}$$

Where p is the slowness value of the direct P-wave, h is the thickness of the continental crust, α_1 is the P-wave velocity in the crust, and β_1 is the S-wave velocity in the crust. The velocity applied depends on whether it is the Ps- or the PPmP- point that is calculated. The latitude and longitude are calculated by using the X value found in equation 19, and the back azimuth. Afterwards the maps are plotted using a bash scrips and the program GMT (Wessel et al., 2013).

The first Fresnel zone is defined as the largest reflecting ellipsoid where all reflected waves that have phase shifts less or equal to pi/2, reach the receiver (Pearce and Mittleman, 2002). Geometry is used to calculate the radius of the first Fresnel zone. The time as a function of the location of the crossing point along the Moho, is calculated for each phase. For the Ps- wave, the travel time for the S- wave in the crustal layer is given in equation 20. While the travel time for the P-wave in the mantle layer is given in equation 21. When these are added they form a sort of parabola, and we then use the formula $T/4$, where T is 1s based on the mean value of the Ps- and PPmP wave. It is however important to remember that this value of T is just a reference, and that some of the waves may have smaller and larger values. From this, 0.25 is added to the minimum value, and the crossing points of this added value on both sides of the curve are found. The minimum value shows the crossing point according to Snell's law. The distance between these two points gives a radius of the first Fresnel zone for the Ps- wave that is 18 km, as seen in figure 18 (Sheriff (1980): Eaton et al. (1991)). The first Fresnel zone for the PPmP- wave

is found in the same way, but now the S- wave velocity(β_1) in equation 20 is substituted with the P-wave velocity in the crust(α_1), since the wave reflected is a P-wave. Equation 21 remains the same. The first Fresnel zone for the PPmP- wave is 25 km, as seen in figure 19 (Sheriff (1980): Eaton et al. (1991)).

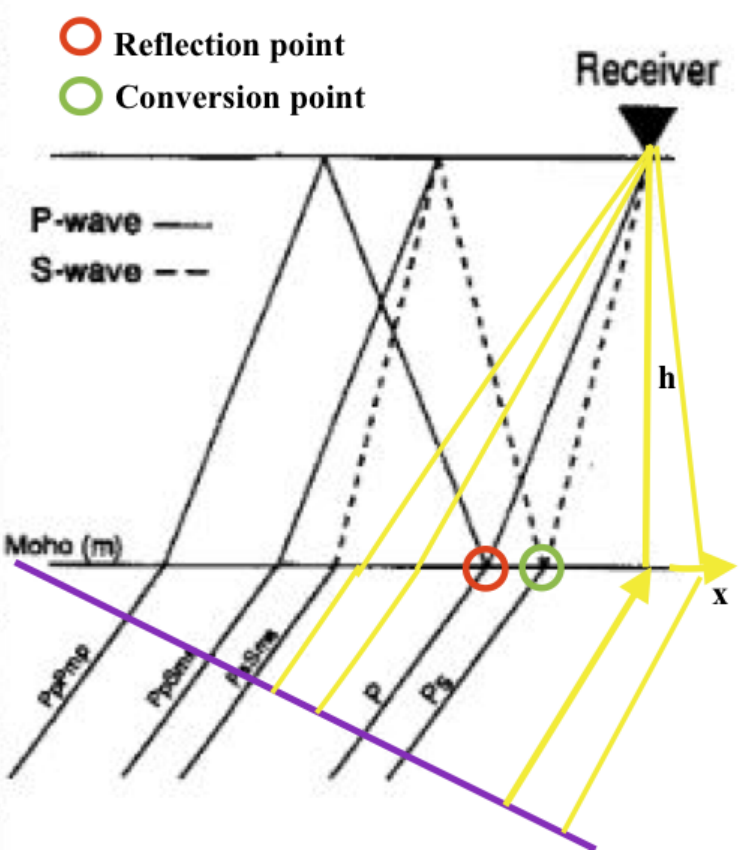

Figure 17: Geometry of the Fresnel zone. The purple line is the incoming P-wave front, and the yellow lines show the waves travelling from the wave front, that do not fulfill Snell's law. The red circle is the point where the P-wave is transmitted and reflected to a P-wave, while the green circle is the point where the P-wave is converted or reflected to a S-wave.

$$t_s = \frac{\sqrt{h^2 + x^2}}{\beta_1} \tag{20}$$

$$t_p = \frac{(A - x)sin(i)}{\alpha_2} \tag{21}$$

Where h is the thickness of the crustal layer, x is the distance along Moho, A is set to 70, i is the angle of the incident P-wave, β_1 are the S-wave velocity in the crust and α_1 and α_2 is the P-wave velocity in the crust and mantle. The sort of parabola that is formed when adding these two travel times, are shown in figure 18 and 19.

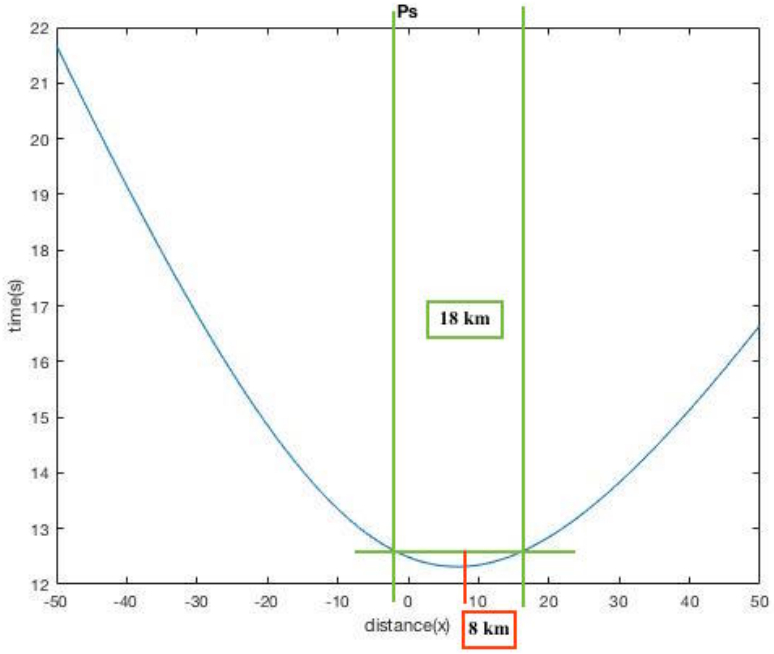

Figure 18: Fresnel zone for Ps- wave. Displays a sort of parabola where 0 km distance is where the seismic station is located. The red line marks where the piercing points hit the Moho, and the green lines displays how the radius was found.

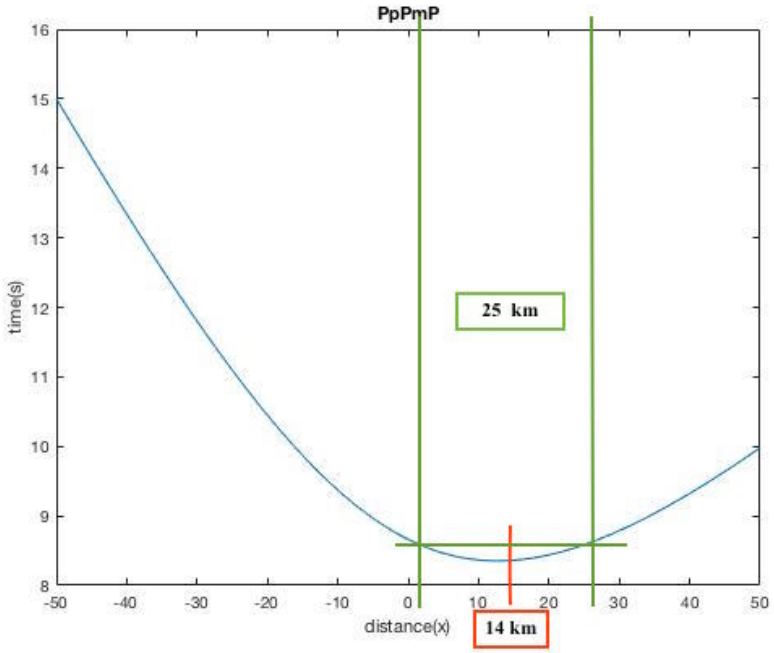

Figure 19: Fresnel zone for PPmP- wave. Displays a sort of parabola where 0 km distance is where the seismic station is located. The red line marks where the reflection points hit the Moho, and the green lines displays how the radius was found.

5 Results

The results show the radial component, also called the receiver function(RF) at the eight Kongsberg array stations and at KONO. The receiver functions were obtained through the steps in section 4. Firstly, the RFs from three separate events, located on different parts of the Earth, are plotted for each of the eight stations. Secondly, the RFs from eight events with various locations are plotted for each station separately, where KONO, KONO1 and KONO5 will be presented. Thirdly, the stacked RFs from the three areas are presented, first by stacking area and then by station. Next, the stacked events from South America are plotted, and the stacked events that are filtered in two frequency intervals in an attempt to remove noise from the data, are listed in Appendix A. Lastly, the maps showing the conversion and reflection points are presented.

KONO7 is missing data in the vertical direction from mid-August 2018 up to 2019, and because we can not deconvolve without the vertical component, the events within this time period are missing. The reason for this data gap is uncertain, but it could be because of a data conversion error. Despite the fact that KONO7 have less available data than the other seven temporary stations, the data are presented with the others for comparison. It is however important to take this into account when the results are presented, because the lack of data from KONO7 may contribute to worse receiver functions.

5.1 Multiple plots

The RFs from three separate events are plotted, where one is from Northern Kuril Island, one from Taiwan and one from El Salvador. The first two are located north and south from Japan, and have a shorter distance between them than they have to El Salvador. The purpose is therefore to identify the difference in RFs that are located in close proximity, and then look at RFs that are located at a greater distance from each other.

5.1.1 One event for all the stations

The eight receiver functions from Taiwan are plotted in figure 20. Figure 20 shows a clear arrival of the direct P-wave at 0s for almost all stations, except for KONO7. KONO7 shows a peak around 0s, but this peak is not as prominent as with the other stations. The signal also has a negative peak at 9s, and from 10s to 30s the signal is elevated

and influenced by noise. KONO5 and KONO6 show shorter periods and the signal is affected by noise after the arrival of the direct P-wave, but can however see a peak at 4s in KONO6. The noise may be caused by the seismic stations' surroundings(see section 4.1). KONO8 also has shorter periods, but shows two small negative peaks at 9s and 22s. KONO1 and KONO2 have similar signals and longer periods, while KONO3 is almost flat after the direct P-wave. KONO4 is the only station that shows a clear positive peak at 4s, that may indicate the arrival of a Ps-wave.

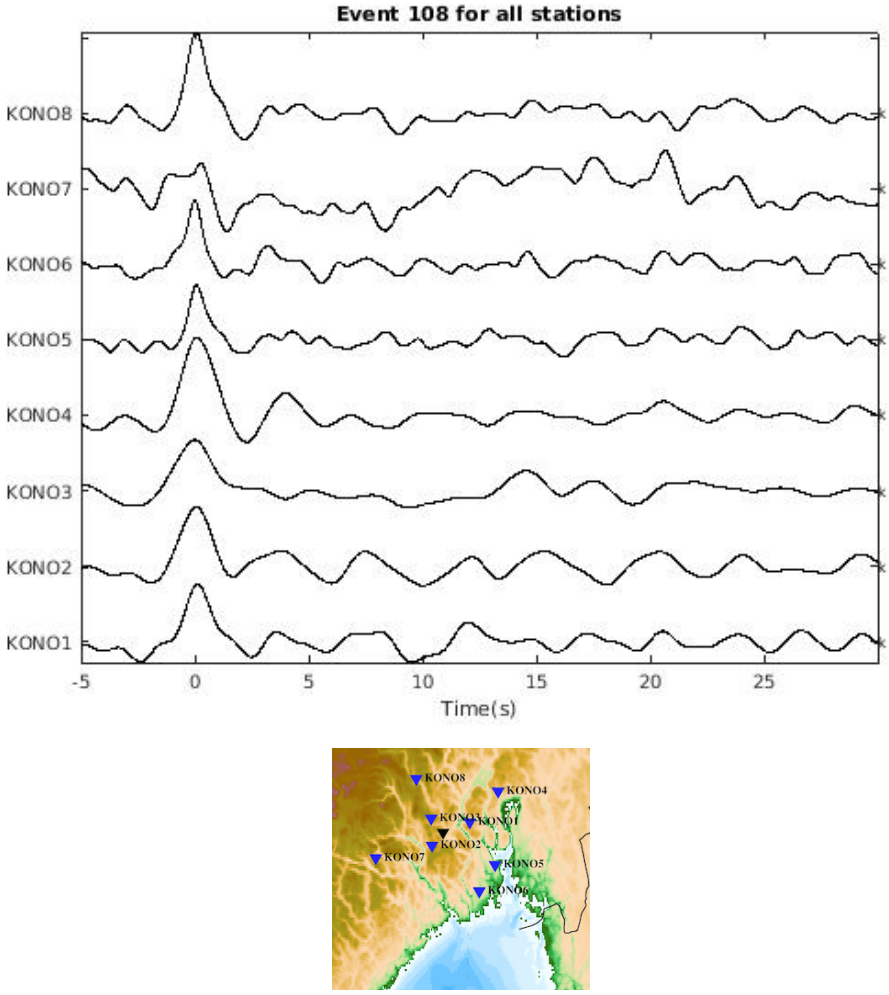

Figure 20: The radial component from event 108 originating from Taiwan for the eight temporary stations. The x- axis shows the direct wave coming in at 0 seconds. Then five seconds before and thirty seconds after are plotted.

The RFs, from the event located at Northern Kuril Island are plotted in figure 21. This event is plotted for KONO in section 4, and due to the good receiver function shown there, it is plotted for the temporary stations in this section. KONO7 is omitted for this event, because of missing data as aforementioned. In figure 21 there is a clear peak at 0s for KONO1, KONO4, KONO5, KONO6 and KONO8. This is the arrival of the direct P-wave. KONO1 has a small peak at 2s, 5s and 12s, and a small negative peak at 10s. KONO2 and KONO3 show no clear arrival of the direct P-wave, the signals have longer periods, and consist mostly of noise. KONO4, KONO5, KONO6 and KONO8 show shorter periods and the signals are influenced by noise.

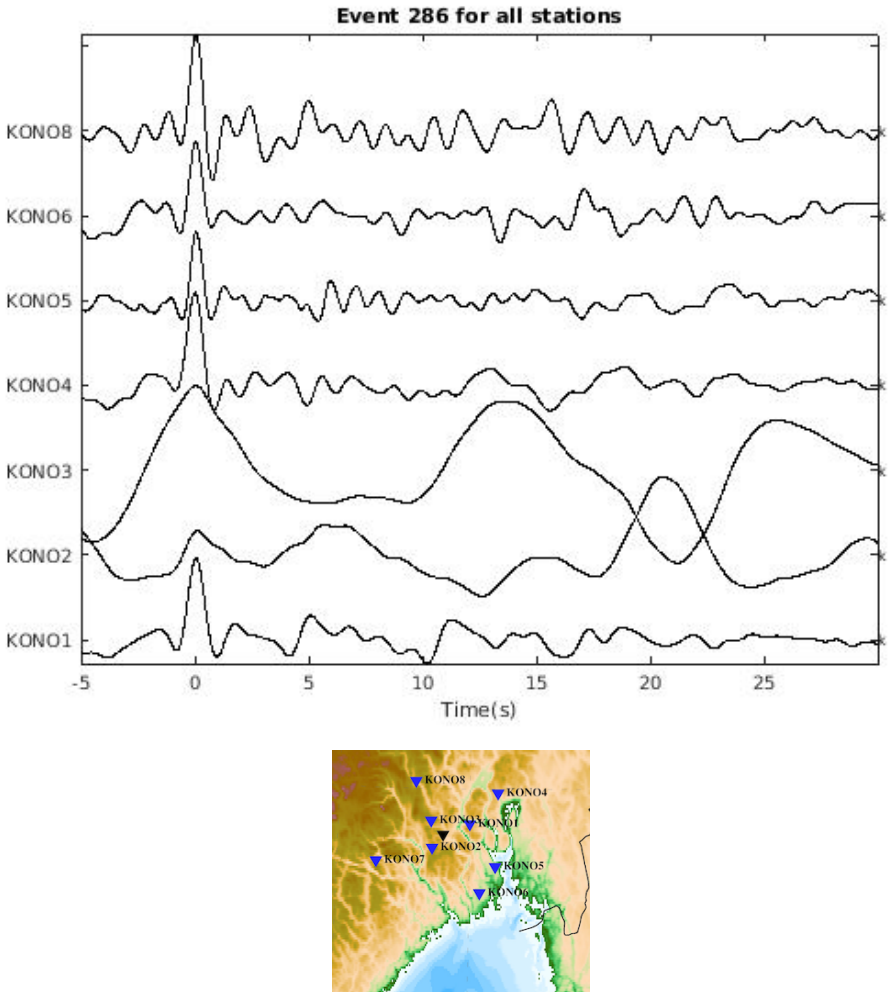

Figure 21: The radial component from event 286, originating from Northern of Kuril Islands for seven of the eight temporary stations. The x- axis show the direct wave coming in at 0 seconds. Then five seconds before and thirty seconds after are plotted.

Figure 22 shows the same as in figure 20 and 21, but for an event located in El Salvador. KONO1, KONO4, KONO7 and KONO8 show the arrival of the direct P-wave at 0s, while KONO2, KONO3 and KONO6 show an earlier arrival at -1s, and KONO5 at -2s. The RFs at all eight stations show high influence by noise, where KONO3 stand out with a higher amplitude in the signal than the other seven. The events show no clear arrivals except for the direct P-wave, but this may be improved by stacking events from this area or filtering out the ambient noise in the data and then stacking. These two methods will be presented later in this section.

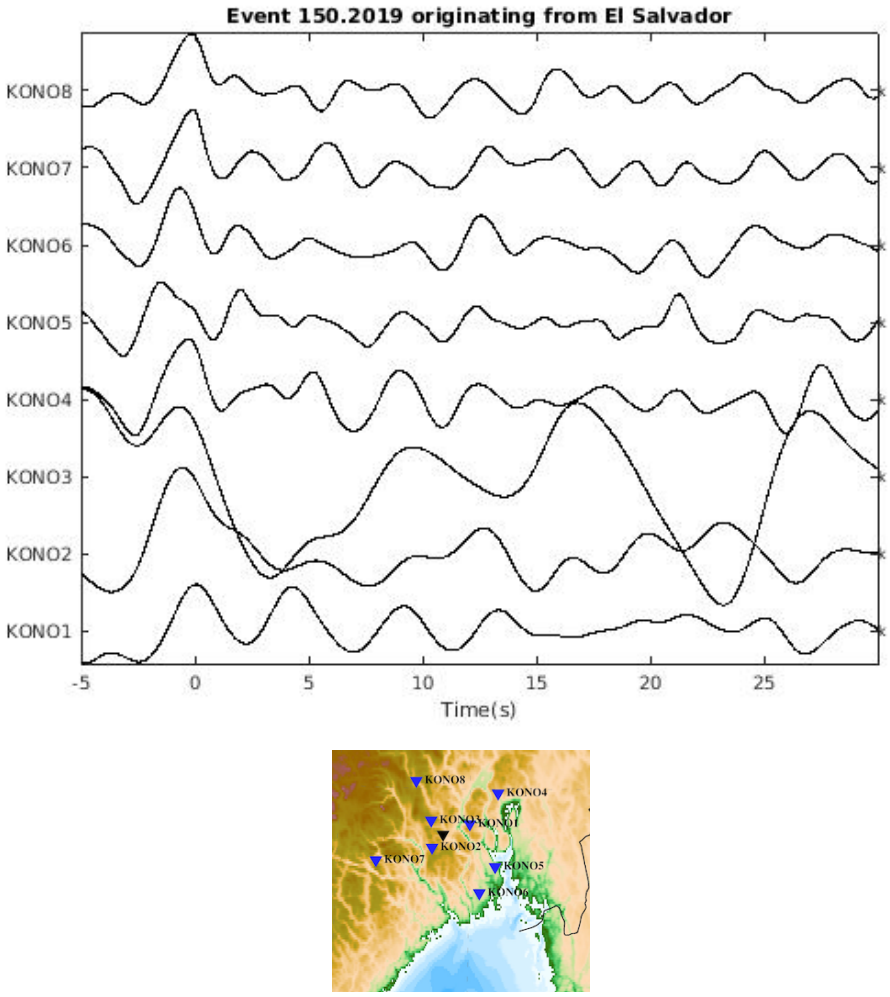

Figure 22: The radial component from event 150 originating from El Salvador for the eight temporary stations. The x- axis show the direct wave coming in at 0 seconds. Then five seconds before and thirty seconds after are plotted.

5.1.2 Different events for one station

Eight events originating from different parts of the world are now plotted for each of the eight stations. In this section the events will be plotted for the permanent station KONO, and the temporary stations KONO1 and KONO5. KONO1 and KONO5 is selected because they lie far away from each other and in different geological environments(see section 2). These receiver functions will give an indication of the signal quality for the two stations, and the correlation between originating area and signal quality. Table

2 provides a list of the eight events plotted in figure 23, 24 and 25. Here the date, magnitude, location and back azimuth is listed.

Day of year, year	Magnitude	Location of the event	Back Azimuth
245,2019	5.9	Northern Mid- Atlandtic ridge	252,1
220,2019	5.8	Afghanistan	93.8
108,2019	6.1	Taiwan	59.85
101,2019	6.0	Off east coast of Honshu, Japan	35.6
365,2018	6.0	Alaska Peninsula	354.65
286,2018	6.7	Nothwest of Kuril Islands	23.9
163,2018	5.9	Southwest of Sumatra, Indonesia	92.4
101,2018	5.5	Near coast of Oaxaca, Mexico	290.65

Table 2: The origin of the eight different events plotted for KONO, KONO1 and KONO5. The Back Azimuth for each event is the median between the Back Azimuth for KONO1 and KONO5.

Figure 23 shows the RFs of the eight different events measured at KONO. Event 101.2018 from Mexico, has a earlier arrival at around -1s, and right after, it sinks into a negative peak of the same size as the positive peak. The other seven events show a positive peak at 0s, indicating a well deconvolved direct P-wave. Event 163.2018 from Indonesia has the weakest signal, with a less prominent arrival of the direct P-wave, and shows small positive peaks at 3s, 6s and 14s. Event 286.2018 from Kuril Island and 220.2019 from Afghanistan have shorter periods, and 220.2019 consists mostly of noise after the direct P-wave. Event 286.2018 show some small peaks from 1-5s, which may indicate the arrival of Ps-wave, and a negative peak at 10s. There are small positive peaks around 3s at event 108.2019 from Taiwan and 245.2019 from the Mid- Atlantic Ridge. Event 101.2019 from Japan shows a clear negative peak at 9s, with two positive peaks at 8s and 12s. Event 365.2018 from Alaska shows a wide direct P-wave peak, which may be caused by scattering of waves. This event also has three small peaks at 3s, 4s and 12s.

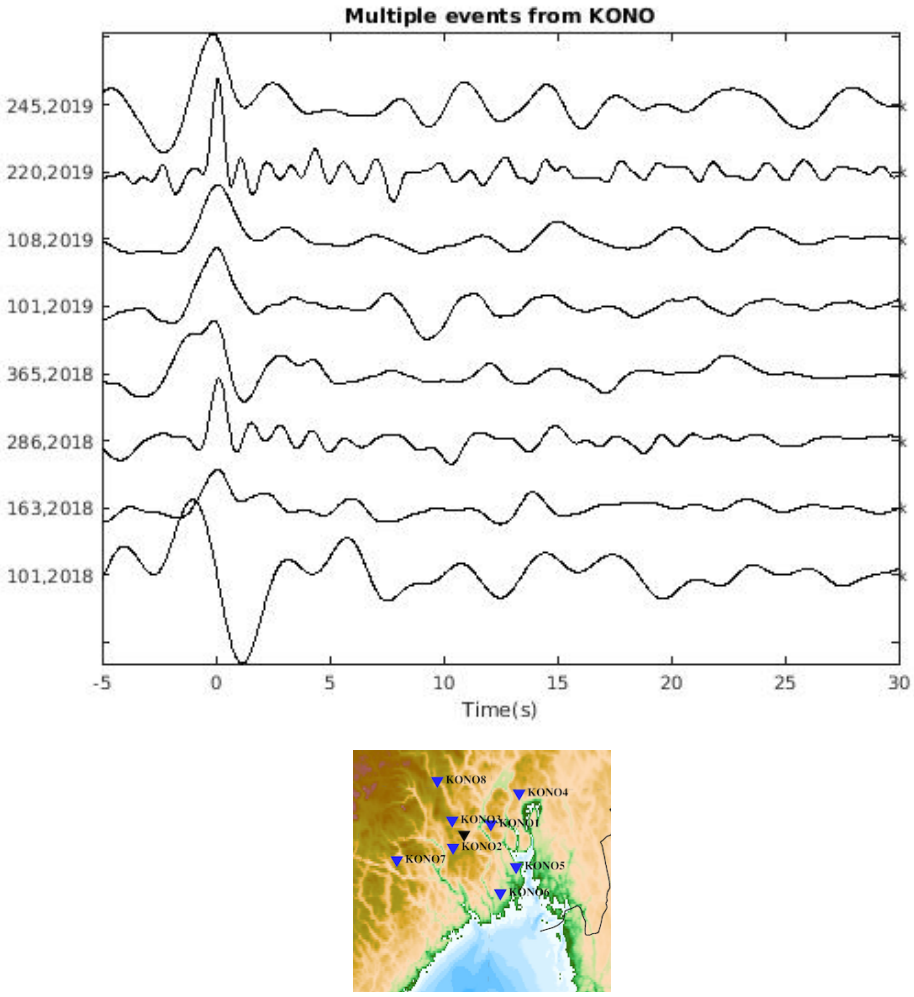

Figure 23: Multiple events from all over the world, measured at KONO5

Figure 24 has many similarities with figure 23. Event 101.2018 from Mexico shows the same early arrival as KONO, around -1s, and the same size negative peak right after. But there are small differences between the stations. Event 365.2018 from Alaska also has an earlier arrival of the direct P-wave, but it arrives a bit later than the previous event at -0.5s. This event also show a small negative peak at 8-9s. Four events have a clear peak at 0s, indicating a well deconvolved direct P-wave, and these events are 286.2018, 101.2019, 108.2019 and 220.2019. The first three of these events, which are from areas surrounding Japan, also show a negative peak at 10s. Event 245.2019 from the Mid- Atlantic Ridge has a small peak at 0s, followed by a small peak at 4s and a negative peak around 6s,

but the signal is highly influenced by noise. Event 163.2018 from Indonesia has a delayed arrival at 1s of the direct P-wave, and two positive peaks at 3s and 6s.

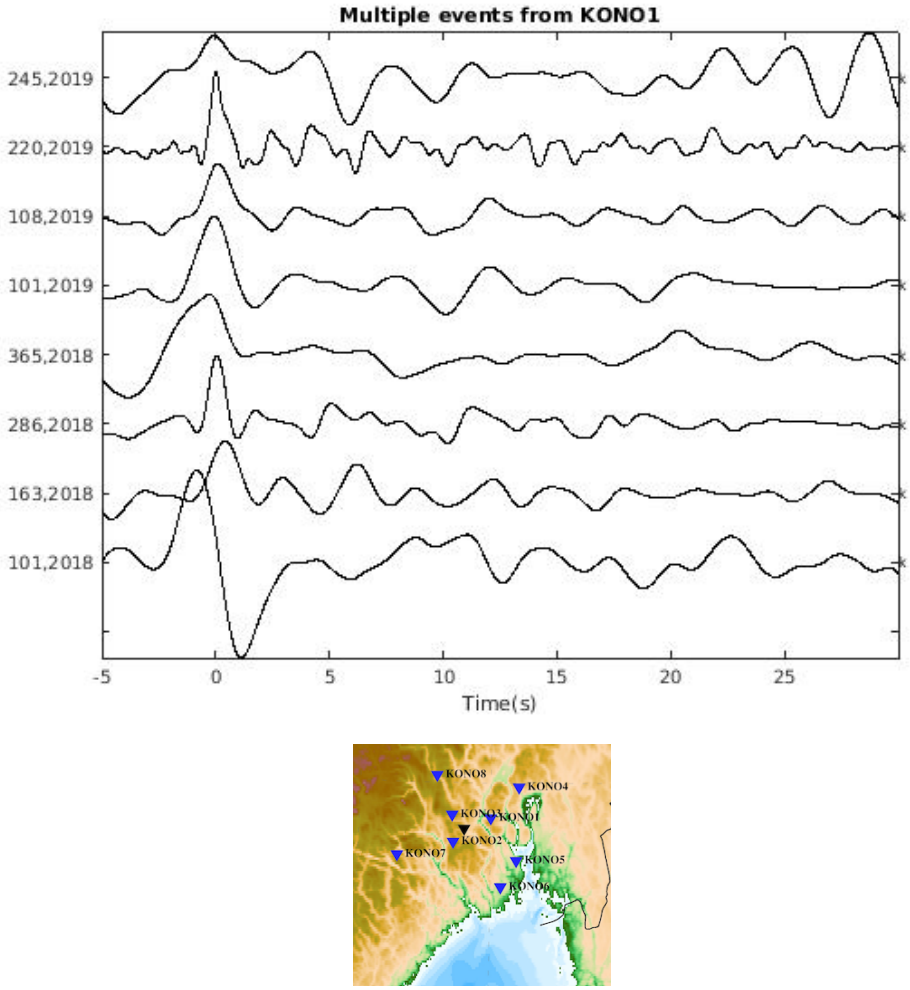

Figure 24: Receiver functions from eight different events, measured at KONO1

Figure 25 shows the results from KONO5, and all eight events contain shorter periods than for KONO and KONO1. Event 101.2018 from Mexico and 163.2018 from Indonesia, does not show a clear arrival of the direct P-wave. The two receiver functions are influenced by noise, and the higher amplitude of event 101.2018 may be influenced by Rayleigh waves caused by the Atlantic Ocean. The six remaining events all have a direct P-wave arriving at 0s, but event 365.2018 from Alaska and 245.2019 from the Mid- Atlantic Ridge have peaks around 0s that does not stand out from the rest of the signal. The amplitude

in event 245.2019 are higher than for event 365.2018, but both consist mostly of noise. Event 286.2018, 101.2019 and 108.2019, all three from the Japan area have a peak at 0s, but have no clear peaks after this. Event 220.2019 from Afghanistan has even shorter periods than the other seven events, but the signal consists mostly of noise.

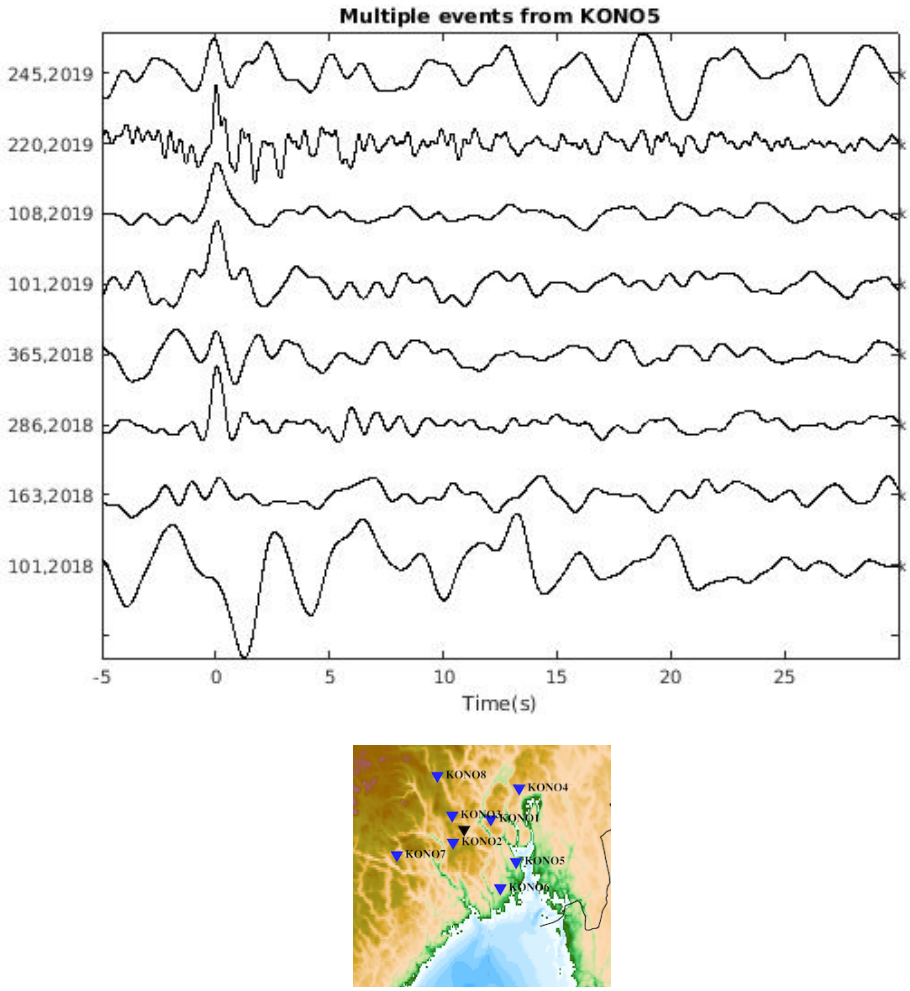

Figure 25: Multiple events from all over the world, measured at KONO5

5.2 Stacking

In this section the events are stacked from three separate areas; Japan, the Philippines and Indonesia, and Alaska and Canada. These three areas are chosen because they have different back azimuth values and have multiple events which form clusters (see section

4.7). Events from South America was also stacked, but when looking at the individual events from South America, and later stacking the events, it became clear that these RFs contain more noise than the other three stacked areas. A way to try and improve this is to filter the data in two frequency ranges and remove the noise between 0.16-0.8 Hz, before adding and stacking them again. Despite trying this method, the result gave bad signals, as shown in Appendix A. The main focus in this section will be the first three stacking areas, where they are plotted first grouped by stacking area, and then grouped by station. The stacked events from South America using one filter will however be presented at the end of this subsection.

When the RFs are stacked, it is expected that the different direct waves and multiples that is present in the separate events will be amplified. This will create a plot with a better view of the significant arrivals that are present in the different areas (Stein and Wysession, 2009).

5.2.1 Stacked events grouped by stacking area

To get a more clear picture of the different areas, the stacked RFs from each area is first plotted for all seismic stations in the same plot. This makes the stations more easy to compare, and to see which of the stations that show less noise and more clear arrivals.

In figure 26 the stacked receiver functions are from the Japan area, and they are stacked separately for the each of the eight stations. All the stations show a clear peak at 0s, which is the direct P-wave. The events that have been stacked here are all events that have receiver functions consisting of short periods, but there are however still differences. In figure 26 there are three groups of periods; KONO5, KONO6, KONO7 and KONO8 show the shortest periods, then KONO1 and KONO4, and finally KONO2 and KONO3 with the longest periods. KONO4 shows a small peak at 2s and a clear peak at around 4s that is 1/3 of the height of the direct P-wave peak, and this is most likely the arrival of the Ps- wave converted at Moho. KONO1 and KONO3 also show a small peak around 4-5s. KONO5 also has a small peak at 2s. KONO2 has an elevated curvature around 5s which may indicate the arrival of the Ps- wave, a negative curvature at 10s, and a positive peak at 12s. KONO1 has a clear negative peak that is about 1/3 of the height of the direct P-wave, and this arrives about 11s after the direct wave, followed by a positive

peak at 12s.

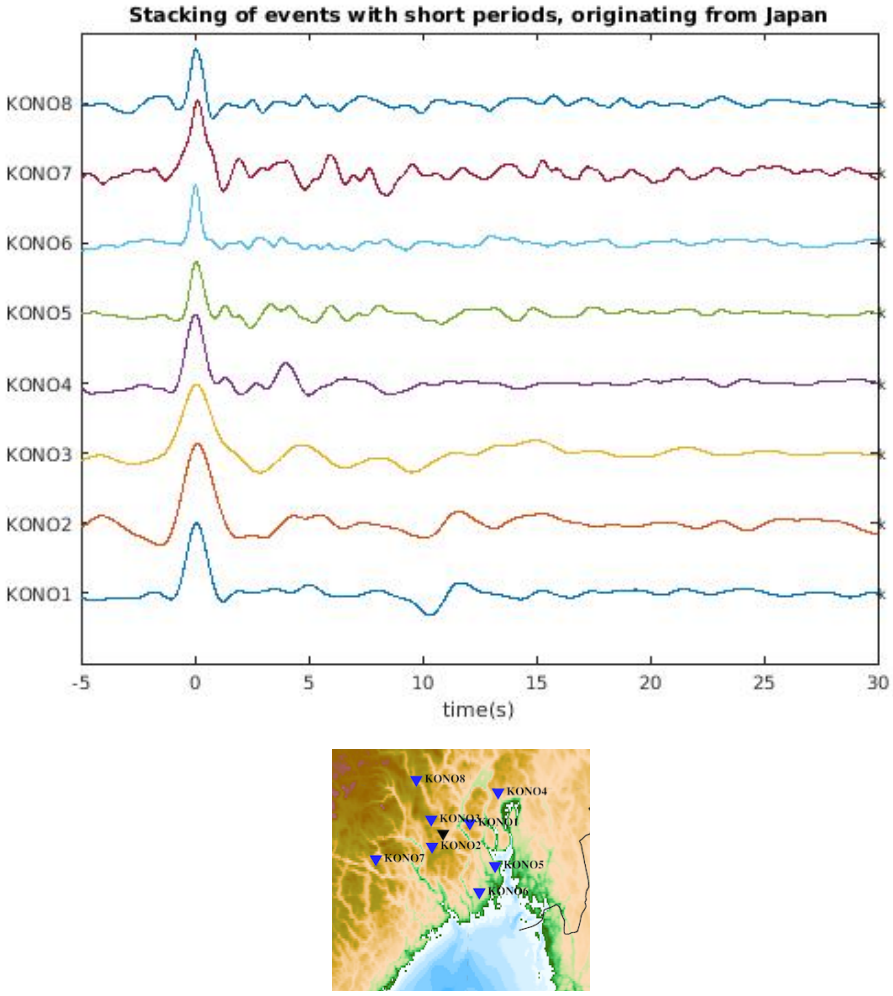

Figure 26: Stacked receiver functions from the Japan area, for each of the eight stations. On the y-axis the different seismic stations are named to their stacked receiver function.

Figure 27 shows the stacked receiver functions from Alaska and Canada, and a clear peak at 0s for the arrival of the direct P-wave for all eight stations. Then at around 4-5s, all stations except for KONO8, show a peak that is about 1/3 of the height of the direct P-wave, and this is most likely the Ps-wave from Moho. This makes the stacked plots from this area more easy to interpret, in terms of figuring out the thickness of the continental crust and the velocity in the two layers. KONO2, KONO3, KONO5 and KONO6 also show a small peak at 2s. KONO5, KONO6 and KONO8 have shorter periods and smaller

peaks, while KONO1, KONO2, KONO3, KONO4 and KONO7 have longer periods and higher peaks. KONO1, KONO3 and KONO4 show a small negative peak around 10s, but these peaks do not stand out when looking at the remaining 20s of the receiver functions.

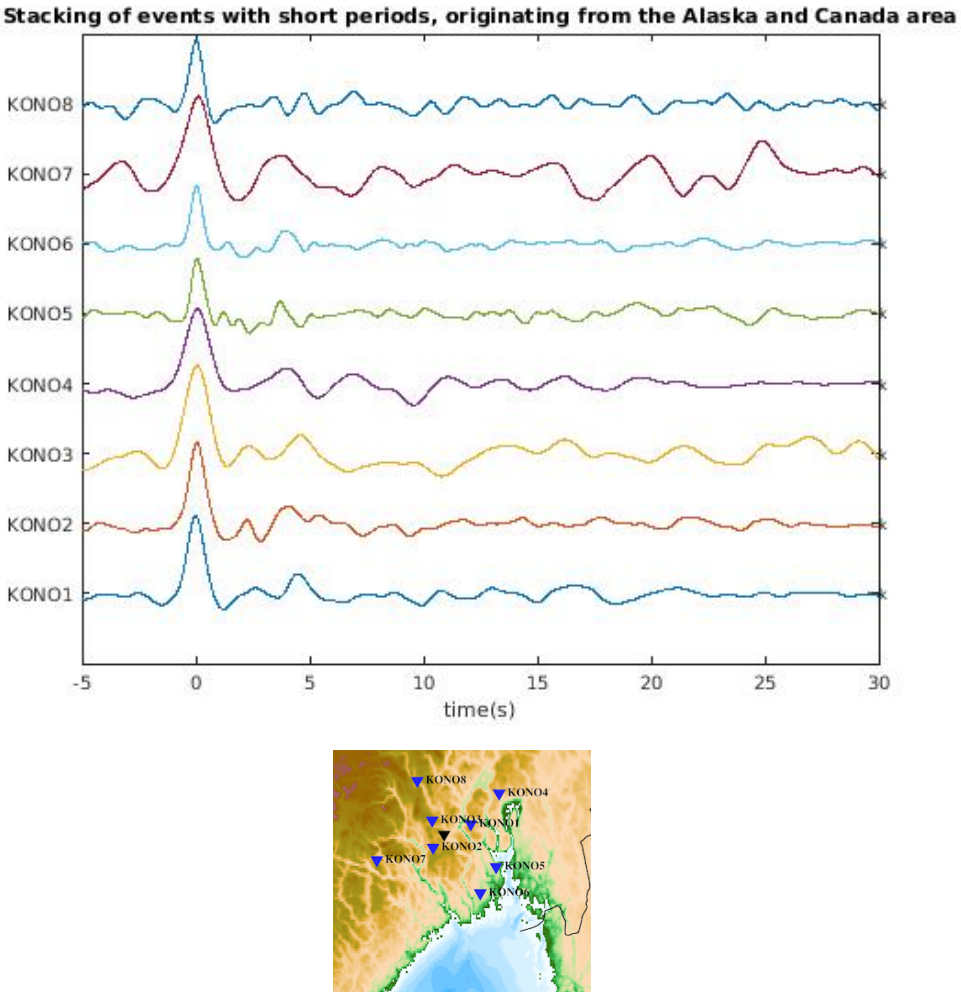

Figure 27: Stacked receiver functions from the Alaska and Canada area, for each of the eight stations. On the y-axis the different seismic stations are named to their stacked receiver function.

Figure 28 shows the stacked receiver functions from the Philippines and Indonesia. The direct P-wave shows a clear peak at 0s, just like the other two plots presented above. The eight stations have similar wave periods, but KONO2 stand out with longer periods. KONO1 and KONO2 show a negative curvature around 10s with two small peaks on both

sides near 8s and 12s, but the peaks are more clear at KONO2. KONO2 also has a small peak at 3s. KONO3 shows a more narrow negative signal, but in this receiver function there are no peaks at the sides. KONO4 shows a positive peak at 4s, a negative peak around 9s, and thereafter a positive peak at 12s. KONO5 and KONO6 are similar, but seem to consist mostly of noise. A small peak at 2s can however be observed in the RF from KONO5. KONO7 shows a lot of noise, but can observe two peaks at 2s and 4s. KONO8 shows a small positive peak at 2s and 5s, and two negative peaks at 6s and 9s that is about half of the height of the direct P-wave.

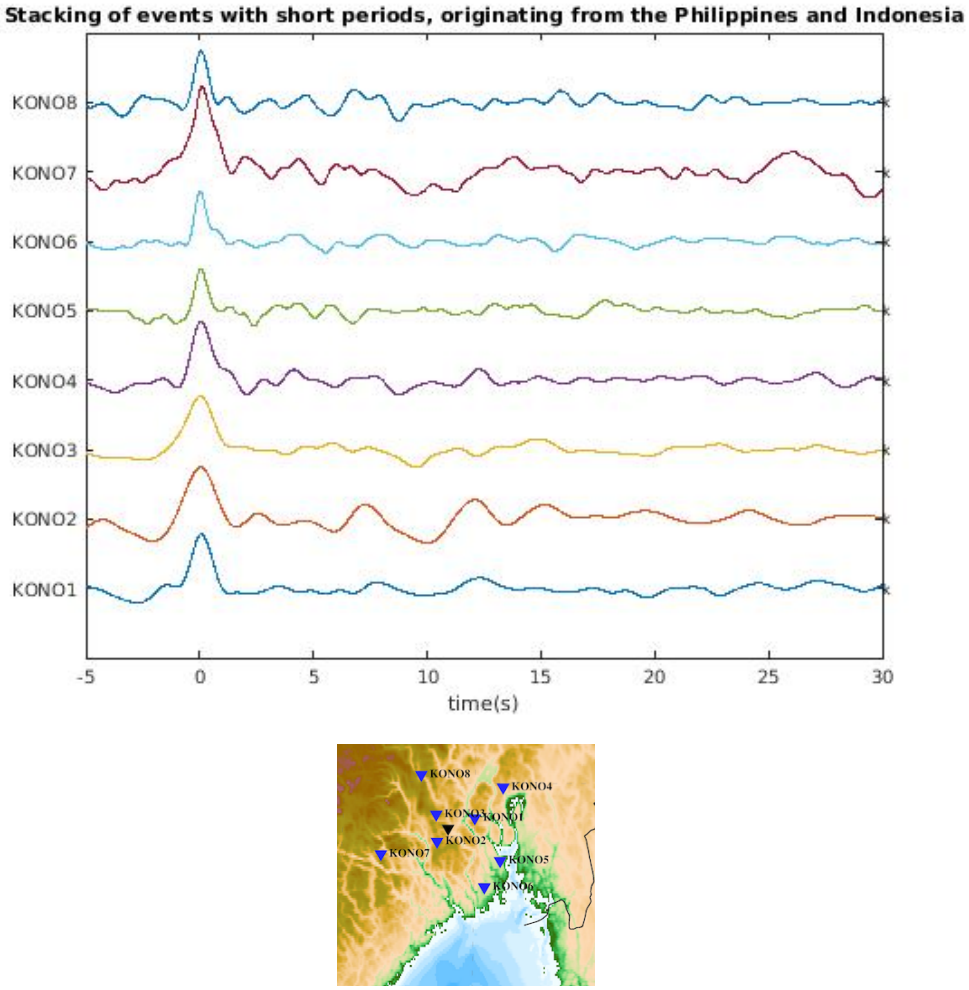

Figure 28: Stacked receiver functions from the Philippines and Indonesia area, for each of the eight stations. On the y-axis the different seismic stations are named to their stacked receiver function.

5.2.2 Stacking from the three areas grouped by station

The focus will now be on the different stations, where all three areas will be plotted for each station. In this section the stacked events from the Japan area is referred to as area J, from the Philippines and Indonesia as area P-I, and from Alaska and Canada as area A-C.

In figure 29 all three areas from KONO1, show a clear peak at 0s, but the amplitude is a little bigger for area A-C. The positive peak at 5s in area A-C is more prominent in this plot than in figure 27, and we can also see a small positive peak at 3s. Area A-C also has three small negative peaks that have about the same amplitude, at 10s, 15s and 19s. Area P-I has as mentioned in the previous section a negative curvature at 10s with positive peaks at both ends at 8s and 12s. We can however also observe a small positive peak at 4s. Area J shows a little peak at 5s that indicates a Ps-arrival, and clear negative peak that is about half the size of the P-wave at about 10s. This is followed by a steep rise and a positive peak at about 12s.

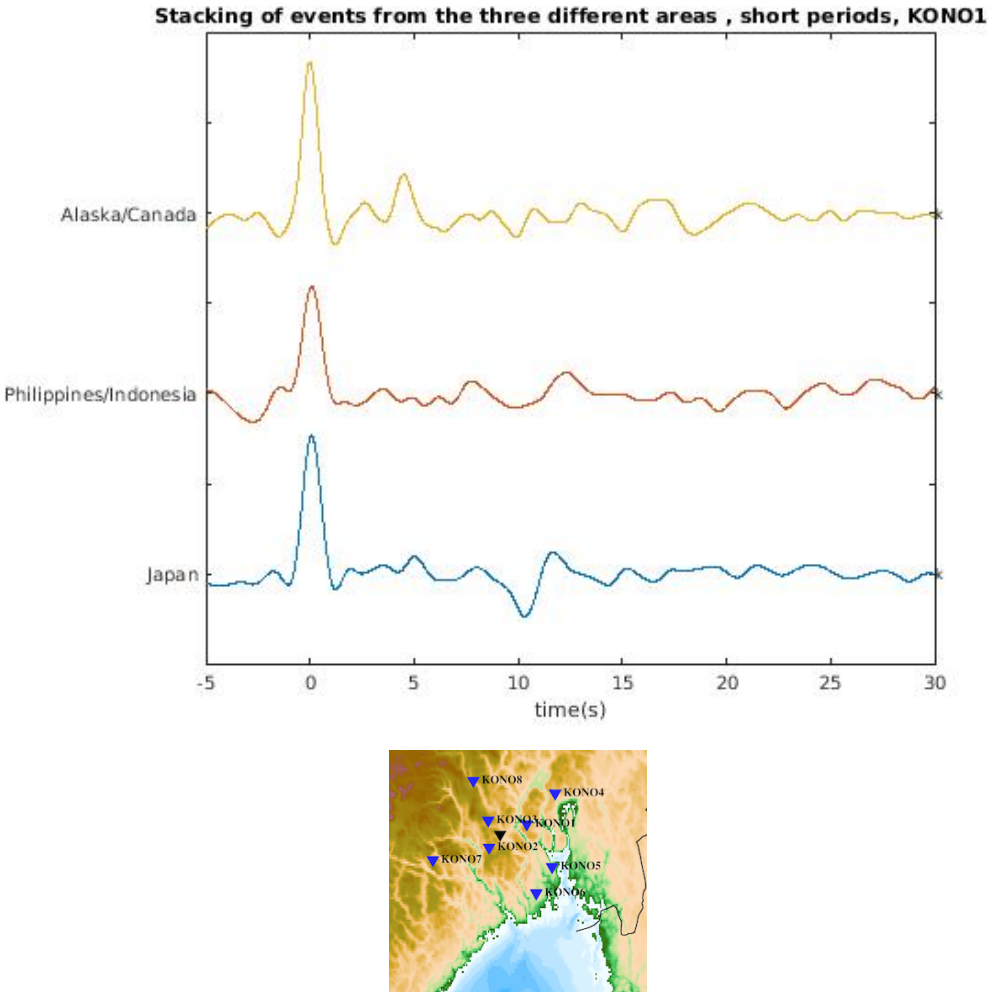

Figure 29: The stacked sections from all three areas, measured at KONO1.

Figure 30 show the stacked sections from KONO2. The peak at 0s is the arrival of the direct P-wave for all three areas. Area J shows positive peaks at 5s and 12s, and a small negative peak at 10s. Area P-I shows a small positive peak at 2s, and then a clear negative peak at 10s that is about half the amplitude of the direct P-wave with positive peaks on both sides at 8s and 12s. Next, we can also observe a positive peak at 15s. Area A-C has shorter periods, and show positive peaks at 2s and 4s.

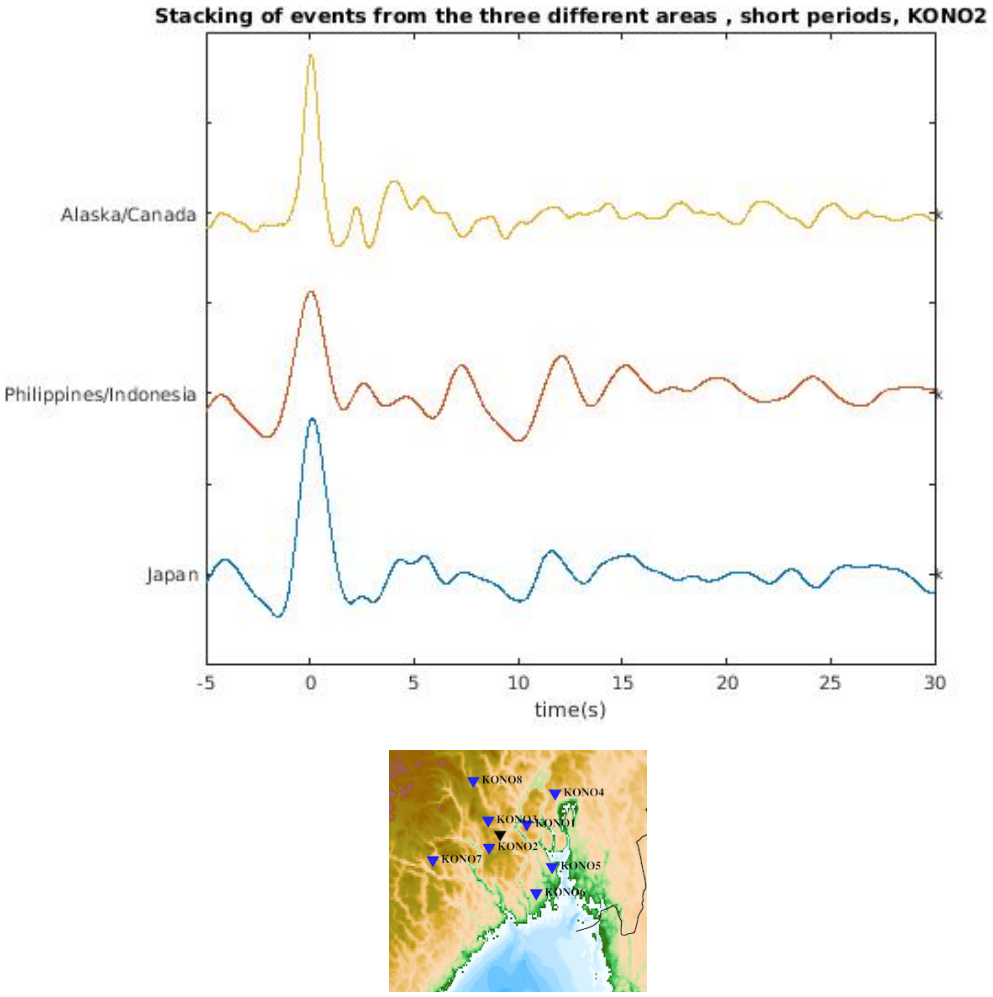

Figure 30: The stacked sections from the three different areas, measured at KONO2

Figure 31 for station KONO3, shows the direct P-wave arriving at 0s. Area J has longer periods in comparison to the other two areas, and has a positive peak at 5s, and thereafter a negative peak at about 10s. This peak is followed by an increase and a positive curvature around 15s. There is also a small positive peak at about 22s. Area P-I has shorter periods and a clear negative peak at 10s. There is also a positive curvature at about 15s. Area A-C shows a small positive peak at 2s, and a higher one at 5s that indicates the arrival of a Ps- wave. There are also two negative peaks at 7s and 11s with a positive curvature in between, and positive peaks at 17s.

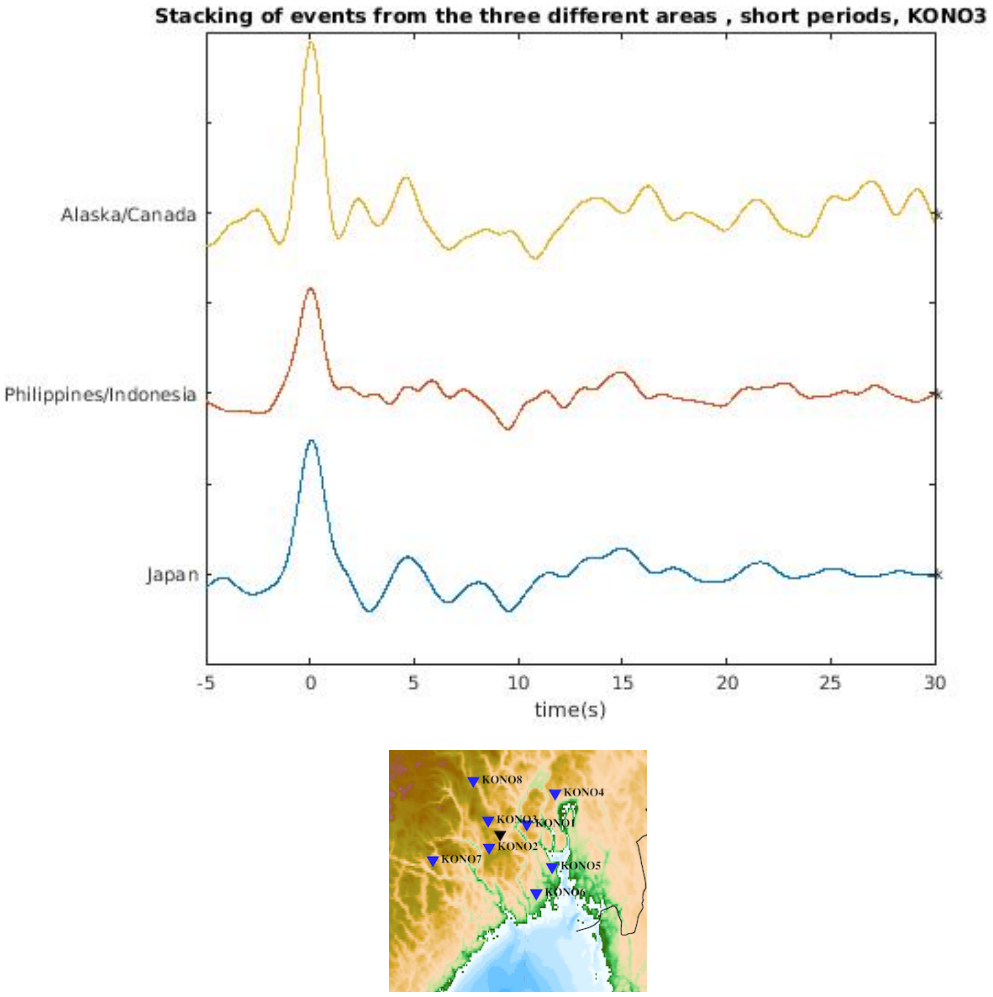

Figure 31: The stacked sections from all three areas, measured at KONO3

In figure 32 for station KONO4, the direct P-wave arrives at 0s. Area J shows a small positive peak at 2s, and a clear positive peak at 4s, that is about half the size of the direct P-wave. There is also a negative peak at 9s. Area P-I shows a small positive peak at about 5s, and then a negative peak at 9s. There is also a positive peak at 12s. Area A-C has two positive peaks at 5s and 7s, and then a clear negative peak at 10s. After this there seems to be noise and then the signal flattens out.

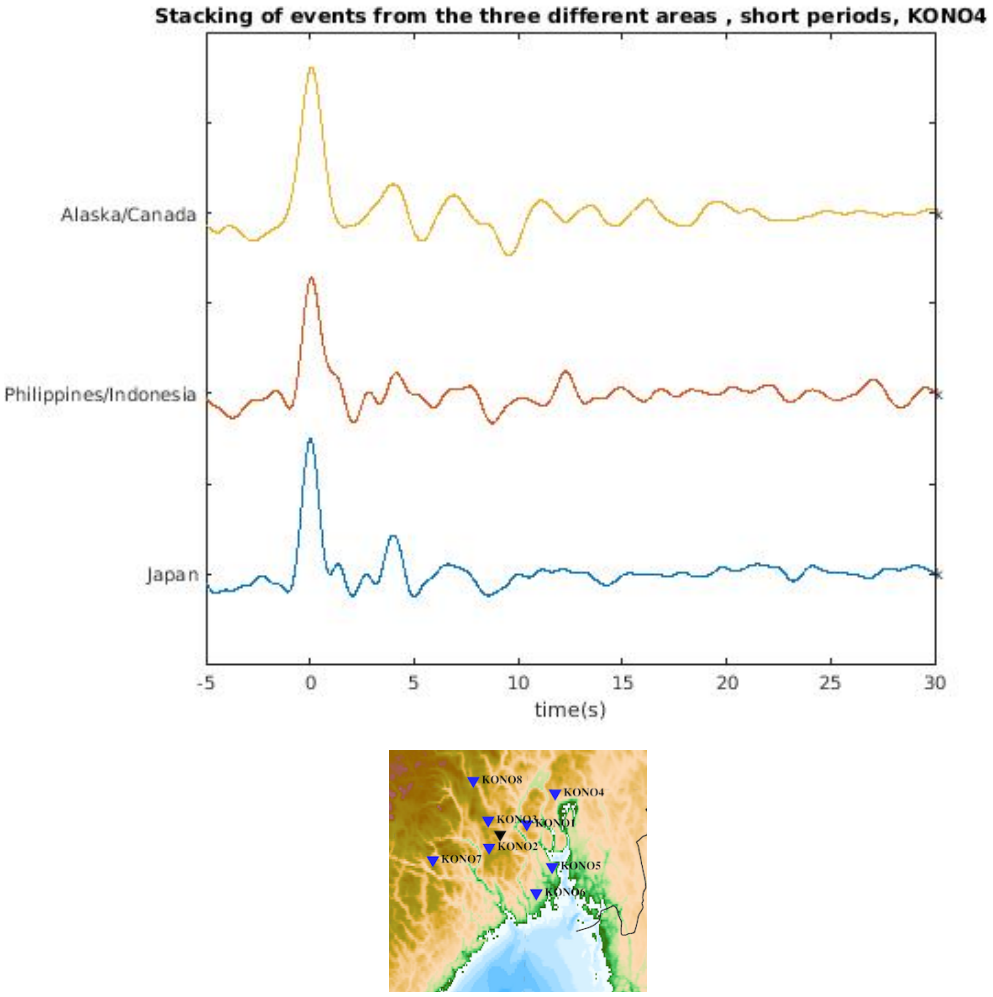

Figure 32: The stacked sections from all three areas, measured at KONO4

Figure 33 shows the stacked sections from KONO5. The three stacked areas show a clear direct P-wave arrival at 0s. All three areas show a small positive peak at 2s, and area A-C shows a clear positive peak at 4s. This peak can also be observed in area J and P-I, but these are not as prominent as in area A-C. After this arrival the signal appears to consist mostly of noise.

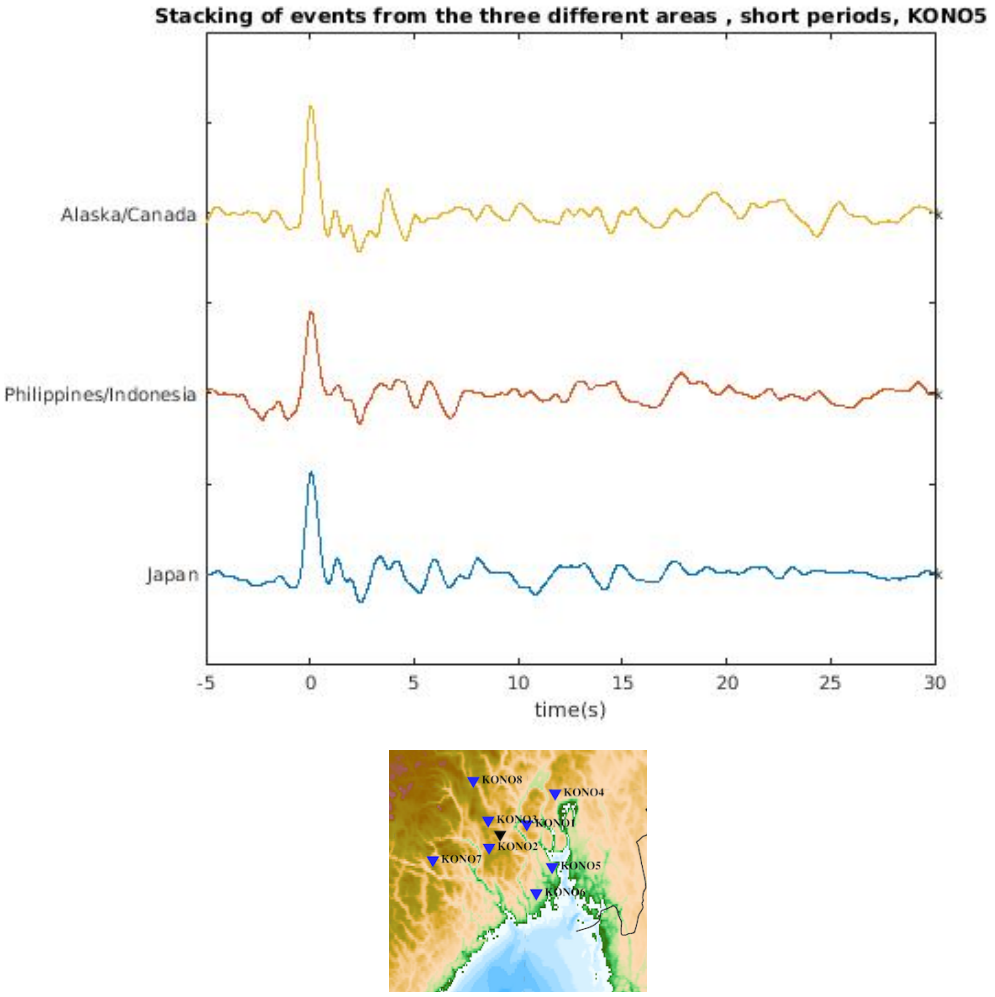

Figure 33: The stacked sections from the three different areas, measured at KONO5

In figure 34 for station KONO6, the direct P-wave arrives at 0s. Area J shows no clear peaks after the direct P-wave, and the signal seems to consist mostly of noise. Both areas P-I and A-C have a small positive peak at 2s and a positive peak at 4s, but the peak at 4s is more prominent in area A-C. After this arrival the signal seems to consists of noise, and shows no clear peaks. The data from KONO6 can be affected by noise from traffic, and it is therefore possible that this is the noise that is observed in these plots.

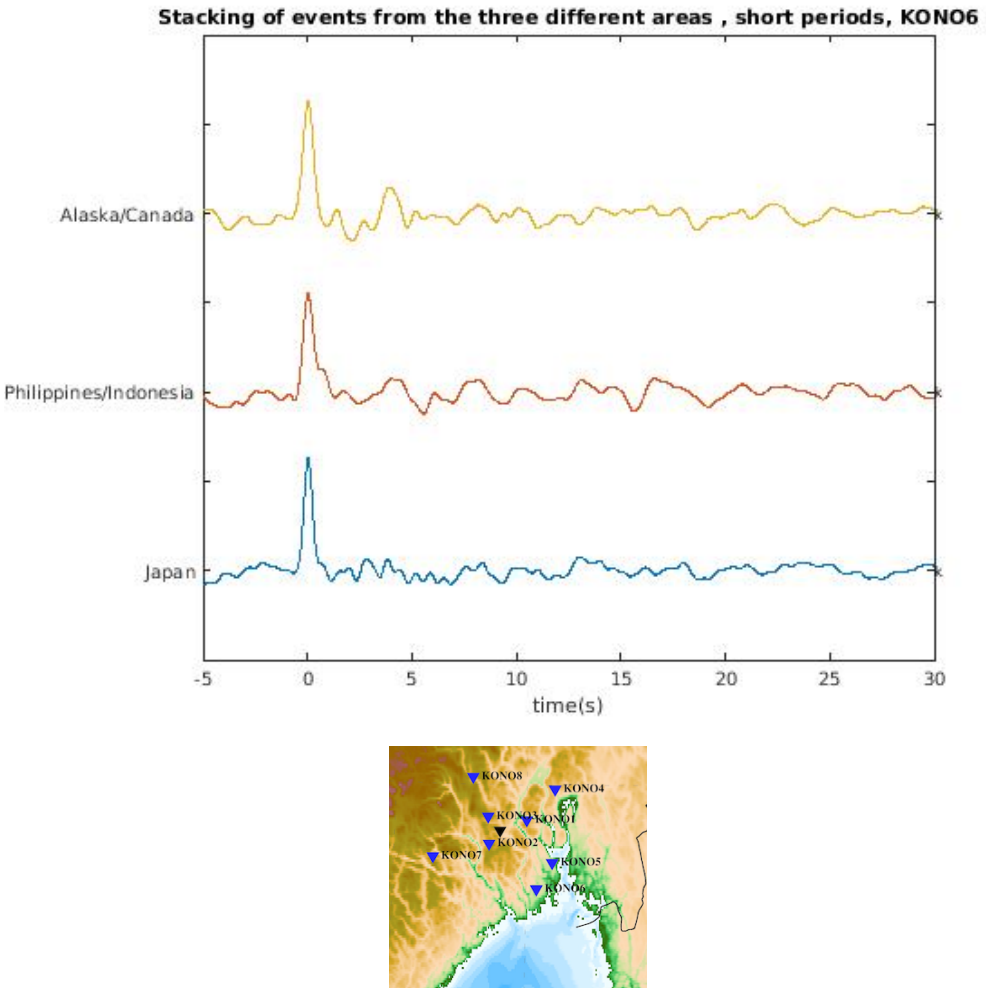

Figure 34: The stacked sections from all three areas, measured at KONO6

Figure 35 shows the stacked sections from KONO7 where technical problems limit the amount of data. All three areas show a clear arrival of the direct P-wave at 0s. Area J exhibit two positive peaks at 2s and 6s. In area A-C there is a peak at 4s, and in area P-I there are two small positive peaks at 2s and 4s. The RFs appear to be very influenced by noise, and this can be because of the goats or carpenter workshop that is located next to the seismometer.

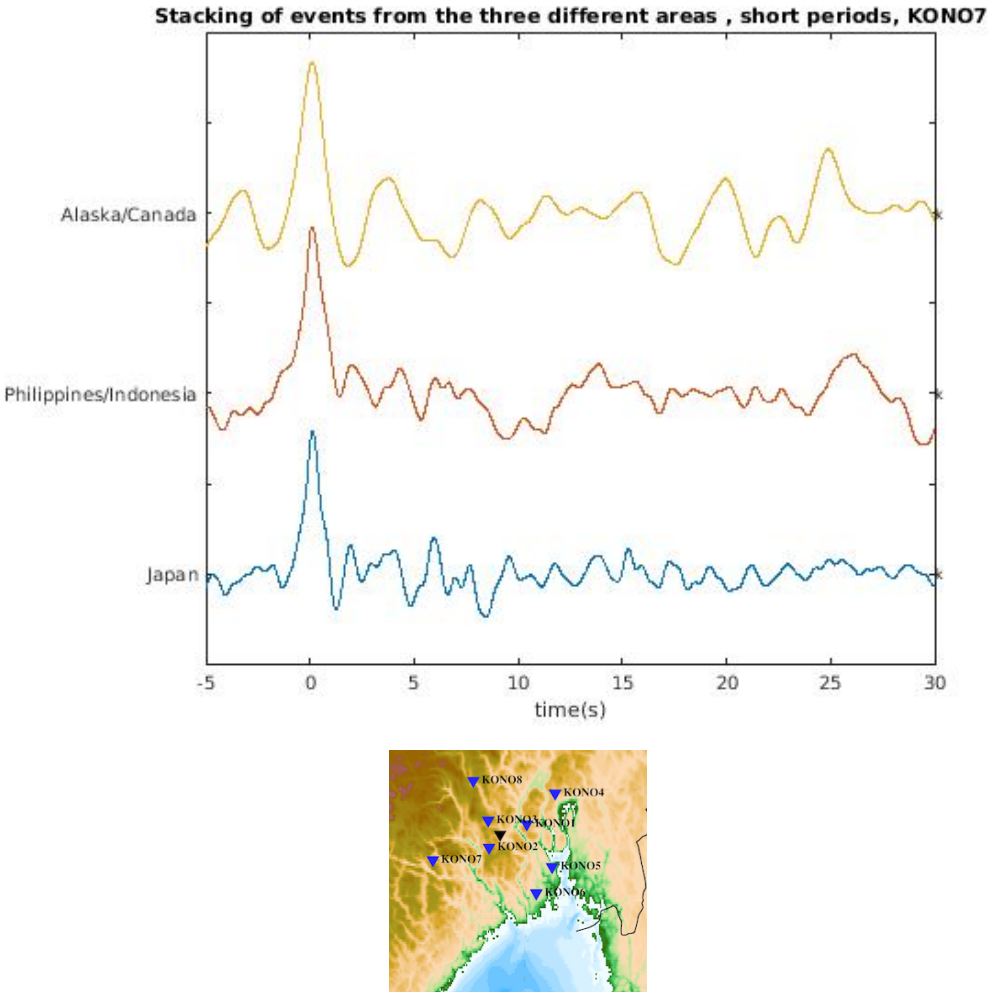

Figure 35: The stacked sections from the three different areas, measured at KONO7

In figure 36 for station KONO8, the direct P-wave arrives at 0s. Both area J and A-C show two small peaks at 5s and 7s, but after this the signal consists mostly of noise. Area P-I has a small positive peak at 2s, 5s and a higher positive peak at 7s. In between the last two positive peaks there is a negative peak at 6s. There is also a negative peak at 9s.

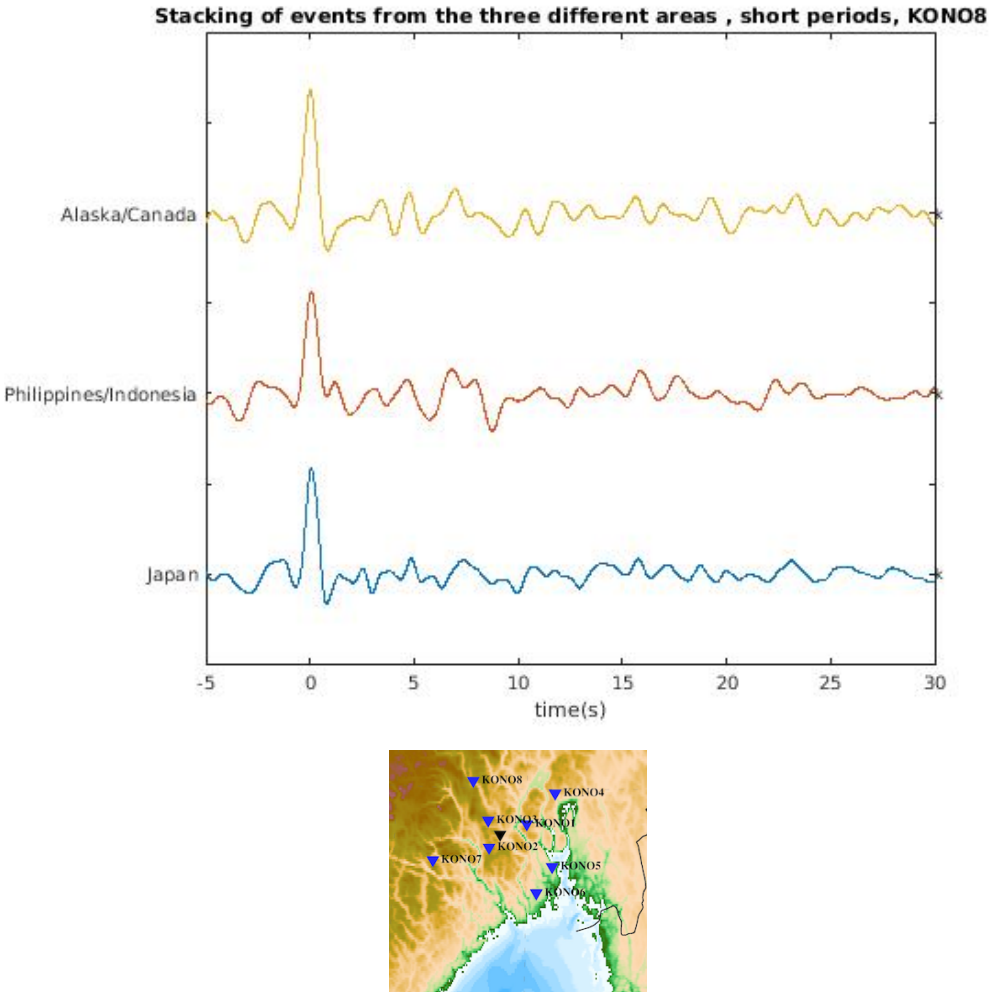

Figure 36: The stacked sections from all three areas, measured at KONO8

Figure 37 shows the three stacked RFs for KONO, which is the permanent seismic station. The direct P-wave arrives at 0s, and is prominent on all three areas. Area J shows two small peaks at 3s and 4s, and positive peaks at 8s, 12s and 15s. There is a clear negative curvature at 10s, that lies in between the peaks arriving at 8s and 12s. Area P-I also shows two small peaks at 3s and 4s, and then two clear positive peaks at 12s and 15s. Area A-C has longer periods than the previous two areas, and show a clear curvatured peak between 4-5s. This area also shows a clear negative peak at 10s, that is also observed in area J. The rest of the signal is rather flat.

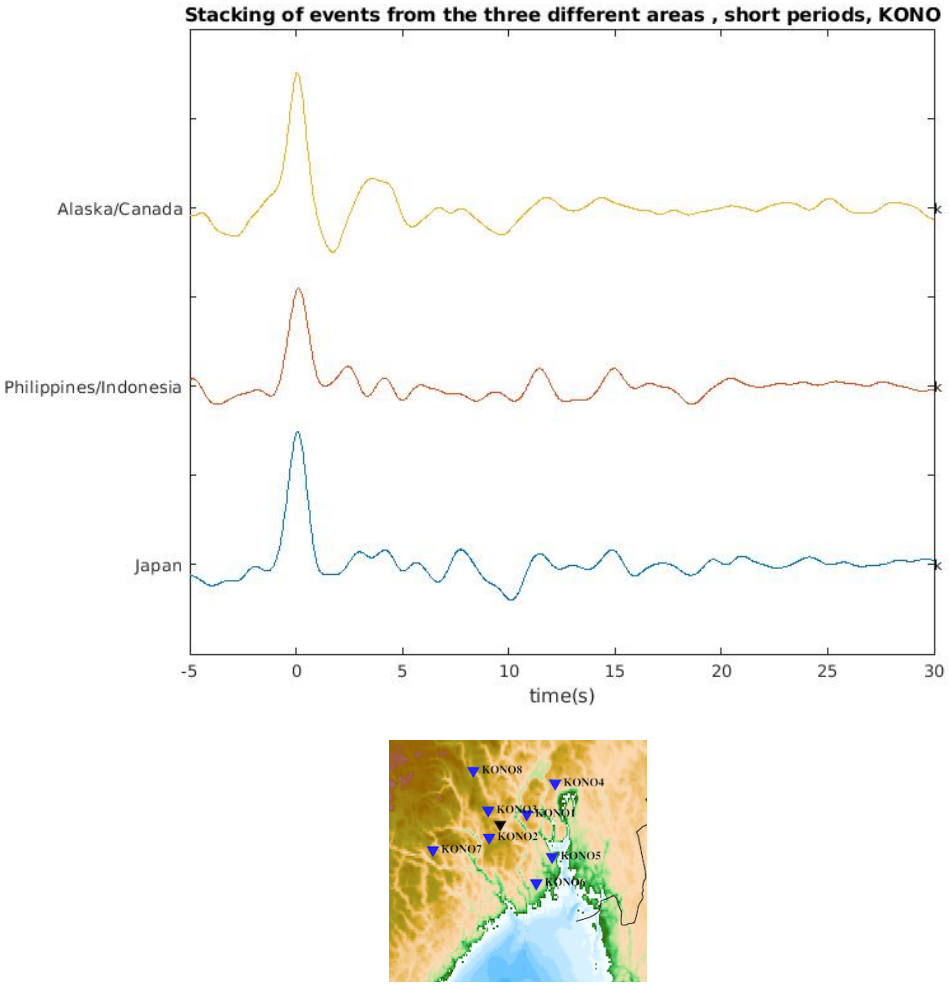

Figure 37: The stacked sections from all three areas, measured at KONO.

5.2.3 Stacking of events from South America

In this section the stacked RFs with the same frequency interval as the other three is presented, and the results from using two separate frequency intervals can be seen in Appendix A.

In figure 38 there is a clear direct P-wave arriving at 0s. KONO5, KONO6, KONO7 and KONO8 show a small positive peak at around 2-3s. While KONO1, KONO2, KONO3 and KONO8 show a positive peak around 5s, and this indicates the arrival of a Ps-wave. KONO1 has a positive peak at 13s, while KONO2 has two negative peaks at 7s and 16s.

KONO5 shows a negative peak at 7s, and a positive peak at 14. KONO4, KONO6 and KONO7 show no clear peaks after the arrival of the direct P-wave. While KONO8 shows negative curvatures around 11s and 14s, with a positive peak at 13s in between, but this may be caused by noise.

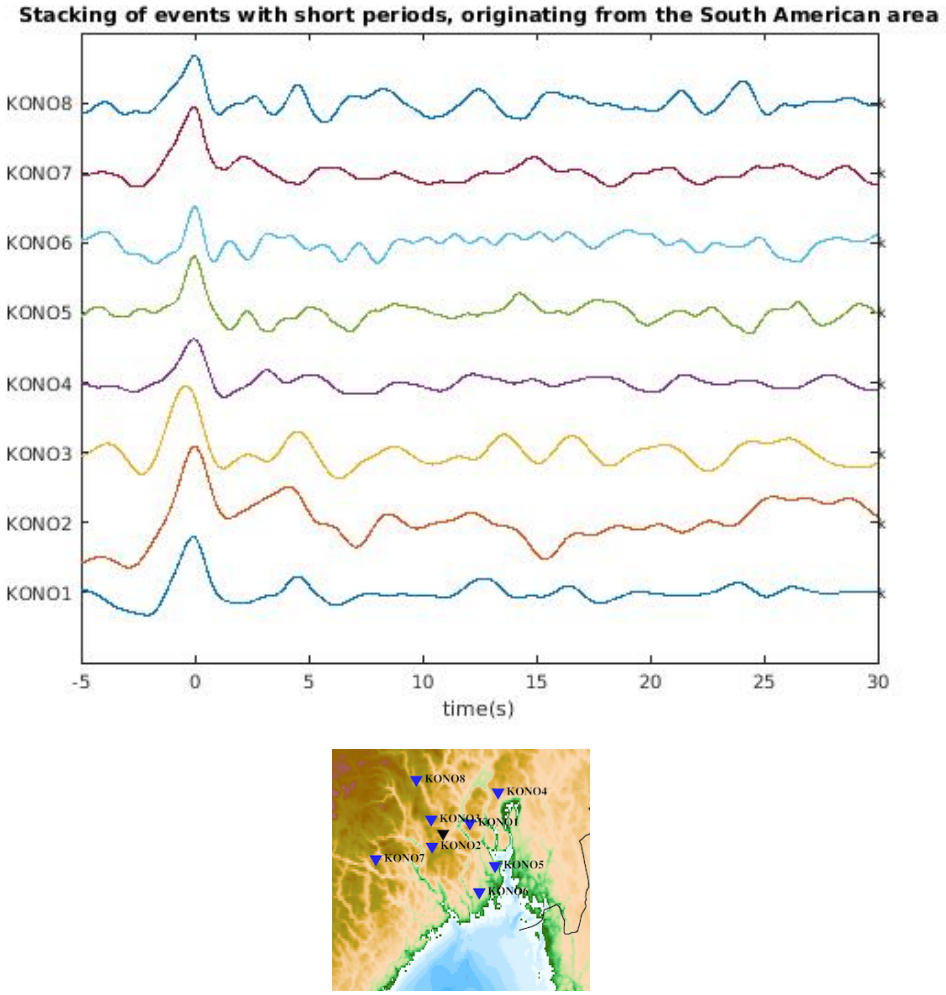

Figure 38: Stacked receiver functions from South America, for each of the eight stations. The signals are filtered with the same frequency range as the other three areas, 0.05 Hz to 3.0 Hz.

The arrivals are not as clear in figure 38 as those observed in the other three stacked areas. To try and improve this, the noise that appears in the frequency range between 0.16-0.8 Hz is removed from the signal, by filtering the signal in two frequency ranges.

Firstly, the signal is filtered with band-pass 0.05-0.16 Hz, then with 0.8-3.0 Hz, and finally they are adding together and stacked (Douglas, 1997).

The results from the stacked RFs with two frequency intervals, as seen in Appendix A, show that this method does not improve the view of the arrivals, and they still have a lot of noise. A different way to try and filter out the noise could be to apply two sets of frequency limits when the instrument response are removed and deconvolved to displacement(see section 4.4), but this has not been tried in this thesis.

5.3 Conversion and reflection points

The location where the Ps- and PPmP waves convert or reflects at the Moho around each of the nine seismic stations, are calculated and plotted using GMT (see section 4.8), and the maps can be seen in figure 39 and 40. In figure 18 and 19 it is found that the distance between the station and converted Ps is 8 km, and between the station and the reflected PPmP is 14 km. This fits well with the distances in figure 39 and 40.

There is an area south of the station that is not represented, and this is because events that will provide points in that direction are not stacked in this thesis. Possible stacking areas would be around the Mid- Atlantic Ridge or the middle east, but there were fewer events from these areas within the time frame, and therefore this was not done. The events from South America is however included, although the results are more uncertain in this direction.

Figure 39 shows the piercing Ps- points around the nine seismic stations. It can be observed that some of the points at KONO2 (light green) and KONO3 (green) overlap with KONO (red). The other stations are further away, and do not overlap with the other stations.

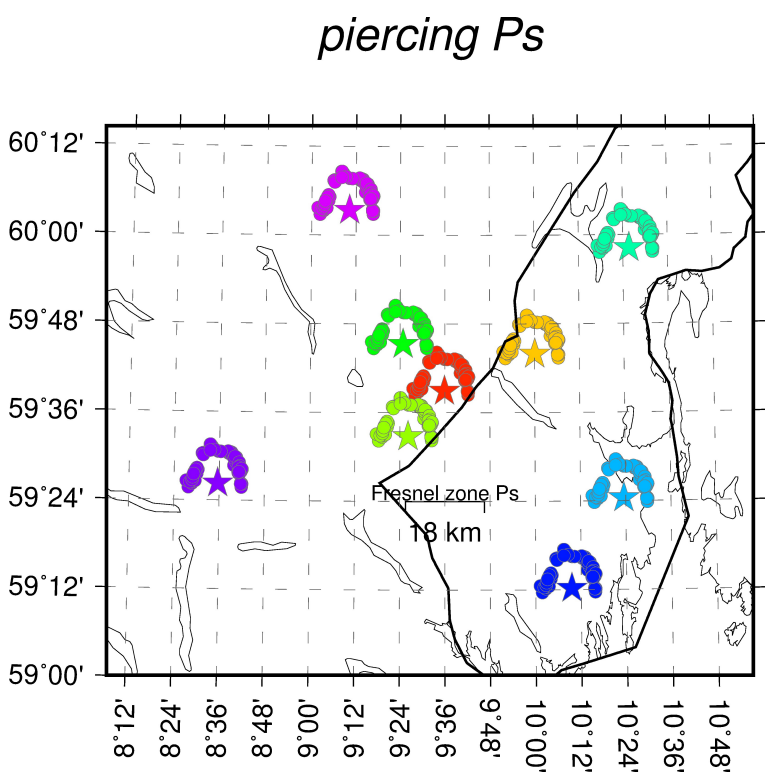

Figure 39: The map shows all piercing Ps- points for KONO (red), KONO1 (yellow), KONO2 (light green), KONO3 (green), KONO4 (turquoise), KONO5 (light blue), KONO6 (dark blue), KONO7 (dark purple), KONO8 (light purple).

Figure 40 shows the reflection PPmP- points around the nine seismic stations. These points show more overlap than the piercing Ps- points. We can observe that KONO1 (yellow), KONO2 (light green) and KONO3 (green) all have overlapping points with KONO (red). Some of the points at KONO2 (light green) that originate from Japan and the Philippines and Indonesia also overlap with the position of the seismic station KONO. Further, we can observe that KONO5 (light blue) and KONO6 (dark blue) have points that lie very close, but they do not overlap. The other stations however, are further away from the other stations and do not show any overlap.

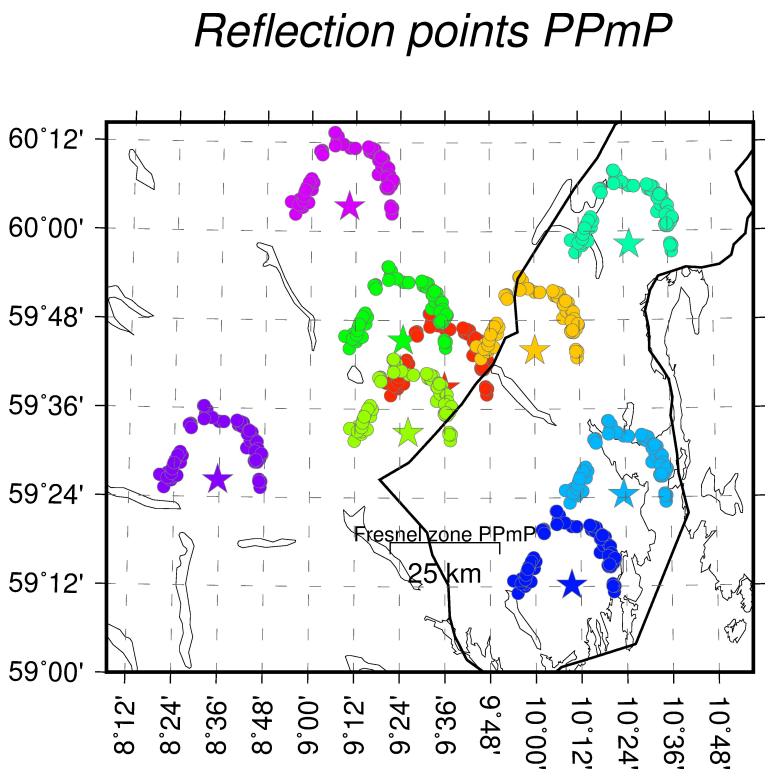

Figure 40: The map shows all reflecting PPmP- points for KONO (red), KONO1 (yellow), KONO2 (light green), KONO3 (green), KONO4 (turquoise), KONO5 (light blue), KONO6 (dark blue), KONO7 (dark purple), KONO8 (light purple)

Table 3 shows which RFs that display clear arrivals of the Ps- wave around 4s and which display the possible PPmP- wave around 10s. The four stacked areas Japan (J), Alaska and Canada (A-C), Philippines and Indonesia (P-I) and South America (SA) are listed as either good, medium or bad according to their visibility in the RFs.

Station	Ps good	Ps medium	Ps bad	PPmP good	PPmP medium	PPmP bad
KONO	A-C, SA	P-I		J, A-C		P-I,SA
KONO1	A-C, SA		J, P-I	J, P-I	A-C	SA
KONO2	J,A-C,SA		P-I	P-I	J	A-C, SA
KONO3	A-C,SA	J	P-I	J, P-I	A-C	SA
KONO4	J,A-C,P-I	SA		J,A-C,P-I		SA
KONO5	A-C	SA	J,P-I		J	P-I, A-C,SA
KONO6	A-C	P-I	J, SA		P-I	J,A-C,SA
KONO7	A-C		J,P-I,SA		P-I	J,A-C,SA
KONO8	SA		J,P-I,A-C		P-I	J,A-C,SA

Table 3: The visible arrivals of Ps- and PPmP- waves in the stacked RFs from the four areas. The four areas are Japan (J), Alaska and Canada (A-C), Philippines and Indonesia (P-I) and South America (SA).

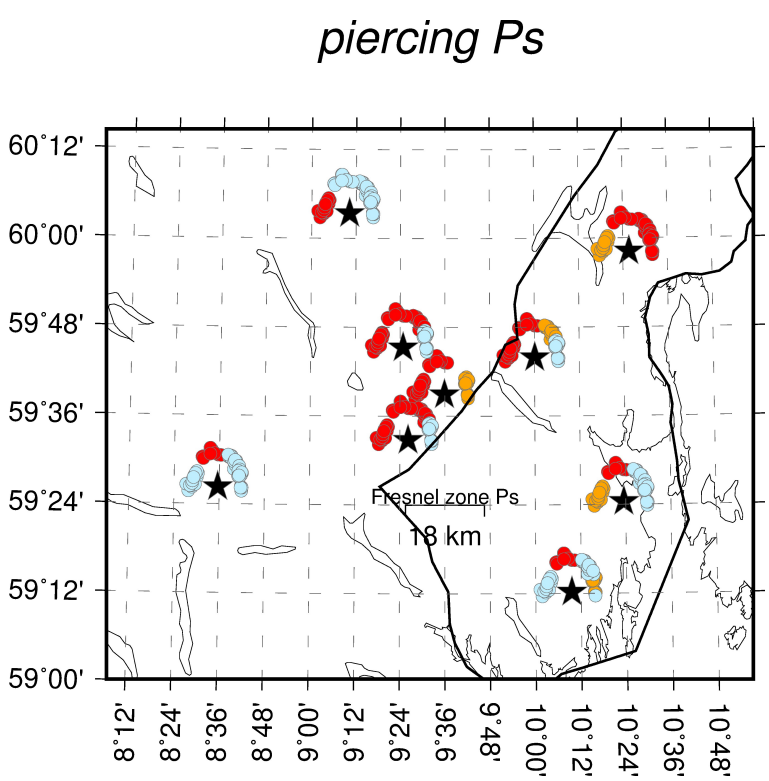

Figure 41: The map shows the events with visible Ps-arrivals in the RFs. The black stars mark the seismic station, the red points display where the Ps-wave is visible, orange when they are somewhat visible, and light blue when they are not visible.

In figure 41 the visible Ps- arrivals are marked with red circles, medium visibility

with orange, and not visible with light blue. The events that originate from Alaska and Canada, and South America show the highest level of visibility on all nine stations, but KONO, KONO2, KONO3 and KONO4 are the stations where the visibility of the Ps-wave is the highest.

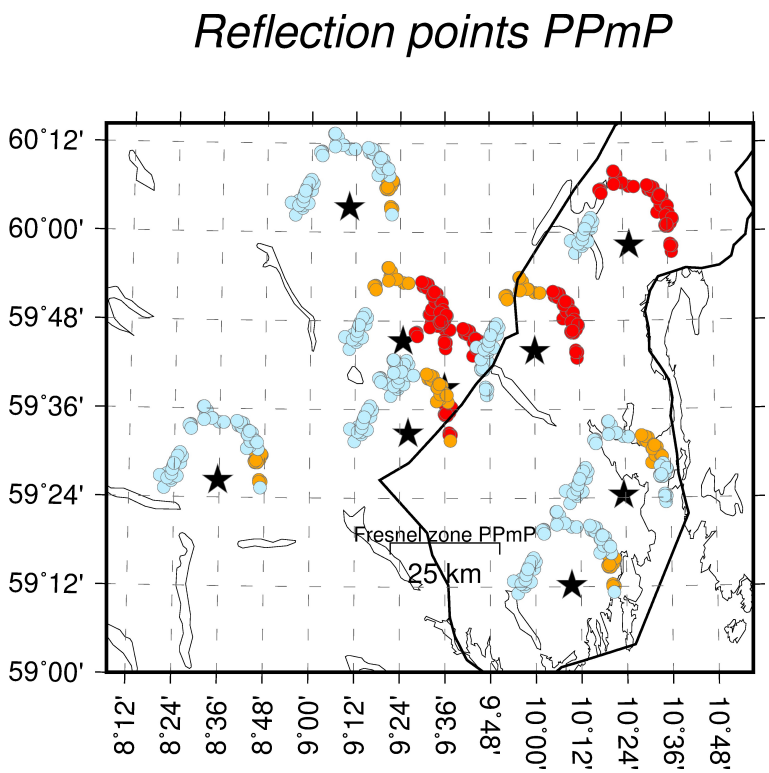

Figure 42: The map shows the events with visible PPmP-arrivals in the receiver functions. The black stars mark the seismic station, the red points display where the PPmP-wave is visible, orange when they are somewhat visible, and light blue when they are not visible.

In figure 42 the points are marked in the same way as in figure 41. The events that originate from the Japan, and the Philippines and Indonesia show the highest level of visibility, where KONO, KONO1, KONO2, KONO3 and KONO4 are the stations where the visibility of the PPmP- wave is the highest.

6 Discussion

The RFs presented in section 6, show mainly the stacked RFs from three different areas. The direct P-wave is clear on all three, which makes the later arrivals and noise easier to identify. The eight temporary stations and KONO show different RFs, where the arrivals of the converted and reflected waves are different. The peaks(arrivals), that stand out on one or more of the stacked areas in each stations arrive at 2s, 4s, 8s, 10s and 12s. These arrivals and what they indicate, will be further discussed in this section. Results from the stacked RFs from South America, seen in Appendix A, show more noise and less clear arrival of the direct P-wave, but some of the results from this fourth stacked area will briefly be discussed and compared.

6.1 What arrival the peaks indicate

From the results in section 6, we can see that there are some observed arrivals after the direct P-wave, that appear in all or most of the stacked RFs. The first is the arrival around 2s, that indicates that there is a boundary that separates the lower and upper crust, and this boundary may be the Conrad discontinuity. This boundary has been thought to separate the granitic and basaltic material in the crust, but this has not been confirmed (Gutenberg (1959): Kanasewich and Cumming (1965)). This boundary is not visible in all areas, because the identification depends on the quality of the seismic data (Kanasewich and Cumming, 1965). Next, there is an arrival at 4s, which has a higher amplitude than the one arriving at 2s. From the calculations done in section 4.7.1 the delay time between the direct P-wave and Ps- wave is around 4s, and this confirms that this peak is the Ps- arrival converted at the Moho. The time delay and the increase in amplitude are in agreement with a primary converted phase (Zhu and Kanamori, 2000). The next arrival is the negative peak at 10s. This peak varies from a very prominent steep peak at KONO1, to a more curvatured form at KONO2, KONO3 and KONO4. The curvatured form can be caused by scattering of waves around the arrival of the multiple (section 3.2). This peak may be the arrival of the multiple PPmP, based on the time they arrive in the RF, but I have no proof that this is the case (Langston (1979): Cassidy (1992)). This is followed by the positive peak at 12s, that is either the arrival of the PpPms, PpSmp or PsPmp (Clouser and Langston, 1995). There is a positive peak at around 8s before the assumed PPmP arrival at some of the stations, and this may be

caused by coda or scattering of waves.

6.2 Comparison of the temporary stations to KONO

The first thing that is noticeable in the RFs from the temporary seismic stations is that they show good results compared to the permanent station KONO. The temporary stations are often of poorer quality compared to the permanent stations, and therefore this differs from the presumed notion that these stations would provide worse results than KONO.

From the stacked RFs plotted for each of the nine stations, one can see that some of the stations show differences between the three stacked areas, while others show similar stacked RFs from all three areas. KONO, KONO1, KONO2 and KONO3 show very different RFs in the three stacking areas. This indicates that these stations are located in areas with a more complicated structure, with possibly a dipping lower crustal layer, dipping Moho, anisotropy or structural heterogeneity. But this could also be a possible result of a mantle reflector at about 65 km depth (Kolstrup and Maupin, 2013). The difference in RFs depending on their back azimuth can also be an indication of scattered waves (Cassidy, 1992). KONO4, KONO5, KONO6 and KONO8 show clear similarities between the three stacked RFs, thereby indicating a more flat horizontal layer. Because these four stations show similar results regardless of the back azimuth, the RFs from the three areas at each station can be stacked together, thereby making the arrivals more clear. Figure 41 does however show that the arrival of the Ps-wave is small at KONO5, KONO6 and KONO8, which may cause the stacking of the three areas to not give a better view of the arrivals.

When plotting the eight different events in figure 23, 24 and 25, the RFs from KONO and KONO1 were highly similar. However, when looking at the stacked receiver functions for all three areas at KONO1 and KONO in figure 29 and 37, there are clear differences. KONO has a clear arrival of the PPmP in the stacked section from area J and A-C, but the arrival is weaker i area A-C. The PPmP arrival, however, is not visible in the RF from area P-I, and this is different from KONO1, KONO3 and KONO4 that all show a PPmP arrival on all three areas.

In the previous research of RFs from KONO, Marianne Kolstrup also observed the unexpected negative peak around 10s. This arrival was found in the RFs with back azimuths between 0-90 degrees. This negative peak is also clear in the P-I and J area at KONO1, KONO2, KONO3 and KONO4, and the events that are stacked in these two areas have a back azimuth value of 15-93 degrees. While the recalculated stacked RFs at KONO from area J also showed a negative peak at 10s, and thereby confirms the results from the previous study. When dealing with a plane horizontal layer, the PPmP-arrival is cancelled out when the signal is deconvolved. This multiple is however visible in the RFs at half of the stations in this thesis, in addition to the study by Marianne Kolstrup. This indicate that there is a layer underneath these stations that do not fulfill these conditions, and thereby the signal is not well deconvolved, because the polarisation of the PPmP is not similar to the polarisation of the P-wave. The layer in question, may be the lower crustal layer that is thicker underneath Oslo Graben, and decreases to the East and West. Which therefore creates a dipping interface at the borders (see figure 3), or it could be a dipping Moho.

KONO, KONO1 and KONO2 lies close to the western border of the Oslo Graben. The different RFs based on their back azimuth at these stations may be a result of scattering by this border (see section 2). In the RFs from area P-I at all three stations(figure 29, 30 and 37), there are some interesting arrivals. At KONO1 and KONO2 there are two clear positive arrivals at 8s and 12s with a negative curvature in the middle. This can also be seen at KONO, but in this case the arrivals are observed somewhat later than at the temporary stations.

KONO3 lies further away from the border, and has the same distance to the Oslo Graben border as KONO4, KONO5 and KONO6, where the three areas show no difference in the RFs based on their back azimuth. But these three stations are located within the Oslo Graben. There is, nevertheless, a long and big fault that seems to cross the area where KONO2 and KONO3 is placed, and may cause the Moho to have a dip (Gabrielsen et al., 2015). This is dependent on how deep the fault goes, as KONO5 is surrounded by multiple small faults which seem to be shallow and not influence the Moho interface. A more likely possibility is however that the lower crustal layer, found in Stratford and Thybo (2011a), might influence the RFs. This layer decreases in thickness over a longer

period to the west, which creates a dipping interface.

The RFs from KONO5, KONO6, KONO7 and KONO8 have little to no similarities to the RFs from KONO. The only similarities seem to be the direct P-wave arriving at 0s, and that the Ps- wave is visible in the stacked RFs from area A-C, with the exception of KONO8. KONO4 has a more similar wave length to KONO, and shows a clear Ps- arrival on all three stacked RFs. The Ps- arrival can also be seen on all three stacked RFs from KONO, but here, the arrival is not as visible as the ones at KONO4. There is however a clear peak in area P-I at 12s which is clear on both KONO and KONO4. The temporary stations that show the most similar RFs with KONO, is thereby KONO1, KONO2 and KONO3. These stations, as seen in figure 1, are the temporary stations that lie closest to KONO.

The Fresnel zones are 18 km for the Ps and 25 km for the PPmP, and this is larger than the distance between the converted and reflected points at the neighboring stations. It would therefore expected to see more similar results between the stations, but this is not the case. All nine stations have different RFs from each other. There are, however, some similarities between KONO5 and KONO6, yet these are small and are not very clear. It can also be observed that the conversion and reflection points in figure 39 and 40 show high degrees of intersections between KONO, KONO1, KONO2 and KONO3. Therefore, the intersection points from these temporary stations can be stacked for KONO in order to attempt to enhance the arrivals.

The stacked RFs at KONO from South America are also highly influenced by noise (figure 44 in Appendix A), just as the temporary stations. In the "one filter", KONO does however show a clear arrival of the Ps-wave, that is similar with KONO1, KONO2, KONO3 and KONO8. In figure 44 and 45, the two different filter methods are applied, and plotted for KONO and KONO1. The RFs show that KONO1 has less noise in the signal. In the "one filter" at KONO1 the Ps- arrival is more clear and we can also observe a peak at 12s, while the "one filter" at KONO shows at more curvatured Ps- arrival. In the "two filters", KONO displays a negative peak at 7s, but this is not clear at KONO1. The Ps- arrival in the "two filters" for KONO1 is however still prominent.

6.3 Crustal layer and Moho

The arrival at 2s, which indicates the Conrad discontinuity, is highly visible at KONO5 and KONO6. At these two stations, the arrival at 2s is sharp and clear in comparison to the same arrival at the other seven stations (including KONO), where this arrival does not stand out in the same way. All nine stations do however show this arrival on one or more of the stacked RFs, and this indicates that the quality of the seismic data is good.

As seen in figure 41, the only station that shows clear Ps- arrivals from all four areas are KONO4. The Ps- arrivals from South America do however have a lower amplitude than the other three areas. The results indicate that the Moho underneath KONO4 has a sharp boundary with a high difference in velocity and density between the layers. Further in figure 41 and 42, where the visible Ps- and PPmP- waves are plotted, there are clear similarities between where these waves are visible in the RFs and what direction the events come from. KONO, KONO1, KONO2 and KONO3 does not show visible Ps- arrivals to the East, but in the same direction the PPmP is visible. A more complex Moho can explain these results. This is however not the case for KONO4, because it lies further away from KONO. Despite the visible PPmP arrival at this station, it also shows good Ps- arrivals in the directions where the PPmP is observed. In the article by Kolstrup and Maupin (2013) the station NWG32 is placed close to KONO4, and this station provided variations in the RFs with back azimuth, and therefore they could not perform the formal inversion. This indicated a more complicated structure, with possibly dipping layers, anisotropy or structural heterogeneity, and could also be because of a mantle reflection at 65 km depth (Kolstrup and Maupin, 2013). KONO4 lies close to NWG32, and the possible PPmP arrival may be caused by the same complicated structure as at NWG32.

The Ps- arrival is however anticipated to be seen in the RFs, while the arrival of the PPmP is not expected to be observed. Therefore, the lack of visibility of the PPmP arrival at KONO5, KONO6, KONO7 and KONO8 does not mean that is does not exist, as it might be hidden by noise. From section 4.1, it was listed that KONO5 may be influenced by noise from a water pipe, KONO6 from traffic and KONO7 from goats and a carpenter workshop, which may cause a lower signal-to-noise ratio.

7 Conclusion

In this thesis, the method P-receiver function(RF) was used to get a better understanding of the continental crust and the Moho boundary underneath the different seismic stations, placed in close proximity or within the Oslo Graben. Based on previous studies of RFs from the permanent station KONO, it was proposed that underneath the station there is a more complicated structure. The RF method was therefore applied to eight temporary seismic stations placed within a 50 km radius of the permanent station KONO, and recalculated for the results from KONO. Instead of stacking all events, cluster events from four different areas where stacked to enhance the arrivals and improve the signal-to-noise radio. Three of the areas provided satisfactory results and was mainly used in this thesis.

The recalculations of KONO concurred with the results found by Marianne Kolstrup, and showed a negative arrival at 10s. This anomaly was also observed in the temporary stations KONO1, KONO2, KONO3 and a weaker arrival at KONO4. Based on the arrival time this may be a PPmP- arrival. The results divided the nine stations into mainly two groups. KONO1, KONO2 and KONO3 showed similar results to KONO, with different RFs depending on their back azimuth. This indicates a more complicated structure beneath the stations. These four seismic stations also show clear Ps- arrivals to the west, and PPmP- arrivals to the east. A more complex Moho can explain these results. KONO4, KONO5, KONO6 and KONO8 showed similar stacked RFs in all three areas, therefore indicating that the ground beneath these stations have a less complicated structure. It is therefore possible to stack all three areas in one for each of the stations to enhance the visibility of the arrivals, and then invert the data. KONO4 did however show Ps- arrivals in all directions, also in the direction where the possible arrival of PPmP was visible. Based on a previous study of a nearby station, this also might indicate a more complicated structure. The results from KONO7 showed similar stacked RFs in the three areas, but because of technical problems, which led to fewer stacked events and lower SNR, this station does not give accurate results.

For future work, it would be interesting to see more results from the station KONO7, that was limited in this thesis due to technical problems. Some temporary stations were

placed by the university of Århus a slighly south of KONO7, and could therefore be utilized for comparison to KONO7. There is also a permanent seismic station at Blindern, called OSL, in the basement of the geology building. This station lies in close proximity to the station KONO4. Therefore, this station could be used to compare the RFs from KONO4, to discern whether they are similar, given that the noise from the city is not too high. Followed by some modelling to see if it's really PPmP that is seen in these arrivals at 10s.

References

C. J. Ammon. The isolation of receiver effects from teleseismic P waveforms. *Bulletin-Seismological Society of America*, 81(6):2504–2510, 1991.

C. J. Ammon. Instrument Response Removal with SAC Pole Zero Files, 2015. URL `http://eqseis.geosc.psu.edu/cammon/HTML/Classes/AdvSeismo/iresp/iresp.html`.

T. Andersen, R. G. Trønnes, and O. Nilsen. Alkaline rocks of the Oslo Rift, SE Norway: A field trip with emphasis on felsic to intermediate intrusive rocks and their associated mineralizations. August 1st to 5th, 2008. 2008.

M. Bath and R. Stefánsson. SP conversion at the base of the crust. *Annals of Geophysics*, 19(2):119–130, 1966.

L. J. Burdick and C. A. Langston. Modeling crustal structure through the use of converted phases in teleseismic body-wave forms. *Bulletin of the Seismological Society of America*, 67(3):677–691, 1977.

J. Cassidy. Numerical experiments in broadband receiver function analysis. *Bulletin of the Seismological Society of America*, 82(3):1453–1474, 1992.

R. W. Clayton and R. A. Wiggins. Source shape estimation and deconvolution of teleseismic bodywaves. *Geophysical Journal International*, 47(1):151–177, 1976.

R. H. Clouser and C. A. Langston. Effect of sinusoidal interfaces on teleseismic P-wave receiver functions. *Geophysical Journal International*, 123(2):541–558, 1995.

A. Douglas. Bandpass filtering to reduce noise on seismograms: is there a better way? *Bulletin of the Seismological Society of America*, 87(3):770–777, 1997.

D. W. Eaton, R. R. Stewart, and M. P. Harrison. The Fresnel zone for P-SV waves. *Geophysics*, 56(3):360–364, 1991.

A. Frassetto and H. Thybo. Receiver function analysis of the crust and upper mantle in Fennoscandia–isostatic implications. *Earth and Planetary Science Letters*, 381:234–246, 2013.

R. H. Gabrielsen, J. P. Nystuen, E. M. Jarsve, and A. M. Lundmark. The Sub-Cambrian Peneplain in Southern Norway: its geological significance and its implications for post-Caledonian faulting, uplift and denudation. *Journal of the Geological Society*, 172(6): 777–791, 2015.

P. Goldstein and A. Snoke. SAC availability for the IRIS community. *Incorporated Research Institutions for Seismology Newsletter*, 7(UCRL-JRNL-211140), 2005.

H. Gurrola, G. E. Baker, and J. B. Minster. Simultaneous time-domain deconvolution with application to the computation of receiver functions. *Geophysical Journal International*, 120(3):537–543, 1995.

B. Gutenberg. *Physics of the Earth's Interior*. International geophysics series. Academic Press, 1959. URL `https://books.google.no/books?id=3RQJAQAAIAAJ`.

M. Heeremans. A plume beneath the Oslo Graben, 2005.

G. Helffrich, J. Wookey, and I. Bastow. *The seismic analysis code: A primer and user's guide*. Cambridge University Press, 2013.

M. Herraiz and A. Espinosa. Coda waves: a review. *Pure and applied geophysics*, 125(4): 499–577, 1987.

E. Kanasewich and G. Cumming. Near-vertical-incidence seismic reflections from the "Conrad" discontinuity. *Journal of Geophysical Research*, 70(14):3441–3446, 1965.

B. Kennett, editor. *IASPEI 1991 Seismological Tables*. Research School of Earth Sciences, Australian National University, 1991.

R. Kind, G. Kosarev, and N. Petersen. Receiver functions at the stations of the German Regional Seismic Network (GRSN). *Geophysical Journal International*, 121(1):191–202, 1995.

M. L. Kolstrup and V. Maupin. A Proterozoic boundary in Southern Norway revealed by joint-inversion of P-receiver functions and surface waves. *Precambrian Research*, 238: 186–198, 2013.

C. A. Langston. Structure under Mount Rainier, Washington, inferred from teleseismic body waves. *Journal of Geophysical Research: Solid Earth*, 84(B9):4749–4762, 1979.

A. Makushkina, B. Tauzin, H. Tkalčić, and H. Thybo. The mantle transition zone in Fennoscandia: enigmatic high topography without deep mantle thermal anomaly. *Geophysical Research Letters*, 46(7):3652–3662, 2019.

Mathworks. Hilbert.Discrete-time analytic signal using Hilbert transformcollapse, R2020a. URL `https://se.mathworks.com/help/signal/ref/hilbert.html`.

F. V. Meinesz. *The Earth's crust and mantle*, volume 1. Elsevier, 2012.

A. E. Mussett and M. A. Khan. *Looking into the earth: an introduction to geological geophysics*. Cambridge University Press, 2000.

National Geographic Society. Ring of Fire, accessed: 11. Mai 2020. URL `https://www.nationalgeographic.org/encyclopedia/ring-fire/`.

Norges geologiske undersøkelse(NGU). Løsmasser. Nasjonal løsmassedatabase, accessed: 10.06.2020. URL `http://geo.ngu.no/kart/losmasse/`.

L. Ottemöller and V. Midzi. The crustal structure of Norway from inversion of teleseismic receiver functions. *Journal of Seismology*, 7(1):35–48, 2003.

T. J. Owens, G. Zandt, and S. R. Taylor. Seismic evidence for an ancient rift beneath the Cumberland Plateau, Tennessee: A detailed analysis of broadband teleseismic P waveforms. *Journal of Geophysical Research: Solid Earth*, 89(B9):7783–7795, 1984.

J. Pearce and D. Mittleman. Defining the Fresnel zone for broadband radiation. *Physical Review E*, 66(5):056602, 2002.

I. B. Ramberg, I. Bryhni, A. Nøttvedt, and K. Rangnes. *Landet blir til: Norges geologi*. Norsk geologisk forening, 2013.

J. M. Reynolds. *An introduction to applied and environmental geophysics*. John Wiley & Sons, 2011.

S. Rondenay. Upper mantle imaging with array recordings of converted and scattered teleseismic waves. *Surveys in geophysics*, 30(4-5):377–405, 2009.

T. Ryberg and M. Weber. Receiver function arrays: a reflection seismic approach. *Geophysical Journal International*, 141(1):1–11, 2000.

M. K. Savage. Lower crustal anisotropy or dipping boundaries? Effects on receiver functions and a case study in New Zealand. *Journal of Geophysical Research: Solid Earth*, 103(B7):15069–15087, 1998.

L. Sawade. Global Common Conversion Point Stacking and its Applications, 2018.

R. Sheriff. Nomogram for Fresnel-zone calculation. *Geophysics*, 45(5):968–972, 1980.

S. Stein and M. Wysession. *An introduction to seismology, earthquakes, and earth structure*. John Wiley & Sons, 2009.

W. Stratford and H. Thybo. Magnus-Rex and the new refraction Moho Map for Southern Norway. Technical report, Department of Geography and Geology, University of Copenhagen, 2009.

W. Stratford and H. Thybo. Crustal structure and composition of the Oslo Graben, Norway. *Earth and Planetary Science Letters*, 304(3-4):431–442, 2011a.

W. Stratford and H. Thybo. Seismic structure and composition of the crust beneath the Southern Scandes, Norway. *Tectonophysics*, 502(3-4):364–382, 2011b.

W. Stratford, H. Thybo, J. Faleide, O. Olesen, and A. Tryggvason. New insights into the lithospheric structure of Southern Norway. *EOS, Transactions American Geophysical Union*, 89(53):554–555, 2008.

W. Stratford, H. Thybo, J. I. Faleide, O. Olesen, and A. Tryggvason. New Moho map for onshore Southern Norway. *Geophysical Journal International*, 178(3):1755–1765, 2009.

J. Tryti and M. A. Sellevoll. Seismic crustal study of the Oslo Rift. *Pure and applied geophysics*, 115(4):1061–1085, 1977.

U S Geological Survey(USGS). Station IU KONO, accessed: 7. June 2020. URL `https://earthquake.usgs.gov/monitoring/operations/stations/IU/KONO/`.

S. van der Lee. Removing the instrument response from a seismogram SAC, Shell scripts, Fortran code, and SOD. Technical report, Incorporated Research Institutions for Seismology(IRIS), 15. August, 2011.

L. Vinnik. Detection of waves converted from P to SV in the mantle. *Physics of the Earth and Planetary Interiors*, 15(1):39–45, 1977.

P. Wessel, W. H. Smith, R. Scharroo, J. Luis, and F. Wobbe. Generic mapping tools: improved version released. *Eos, Transactions American Geophysical Union*, 94(45): 409–410, 2013.

L. Zhu and H. Kanamori. Moho depth variation in Southern California from teleseismic receiver functions. *Journal of Geophysical Research: Solid Earth*, 105(B2):2969–2980, 2000.

A First appendix

The RF's are filtered in two frequency ranges, and then added and stacked. This was an attempt to remove the noise between 0.16-0.8 Hz, and make the arrivals of the different phases become more prominent. After looking at the result from this method, it was concluded that this did not work. The RF's that have one frequency interval will be called "one filter", while the other method with two frequency intervals will be called "two filters".

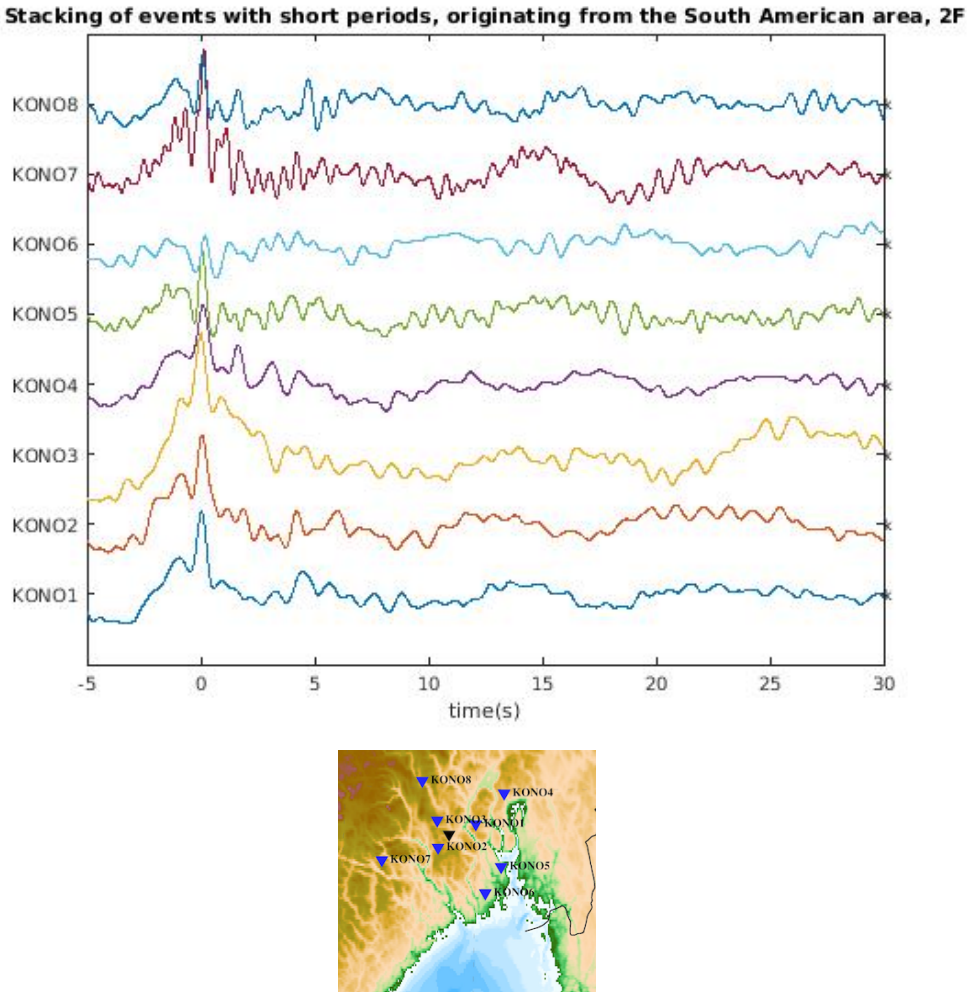

Figure 43: Stacked receiver functions from South America, for each of the eight stations. The signals are filtered with two frequency intervals, to remove the noise that lie in the range of 0.16 Hz to 0.8 Hz.

Figure 43 show the result when this method was used. The stacked RF's show shorter periods and the direct P-wave arriving at 0s. But after the direct P-wave the signal becomes more erratic, and thereby difficult to separate the arrivals from the noise. KONO6 stands out with a amplitude difference in the signal that is lower compared to the other seven. KONO1, KONO2, KONO4 and KONO8 show a positive peak at around 4-5s, and this agrees with the stacked sections in figure 38. KONO4 and KONO8 also show a positive peak at 2s. For comparison the two stacked RF's from South America will be plotted for KONO and KONO1, to see if this gives a better view of the RF's.

Figure 44 compares the "one filter" and "two filters" results at KONO. A clear direct P-wave arrives at 0s. The "one filter" stacked receiver function show a large positive curvature between 3-5s that may be indicating an arriving Ps-wave, but this is not as apparent in the "two filters" RF. After this arrival however the amplitude of the signal drops and becomes more erratic, which indicates the presence of noise. In the "two filters" RF the signal drops after the direct P-wave arrival, and forms a negative peak at 7s. After this the signal increases and stabilise with low amplitude noise.

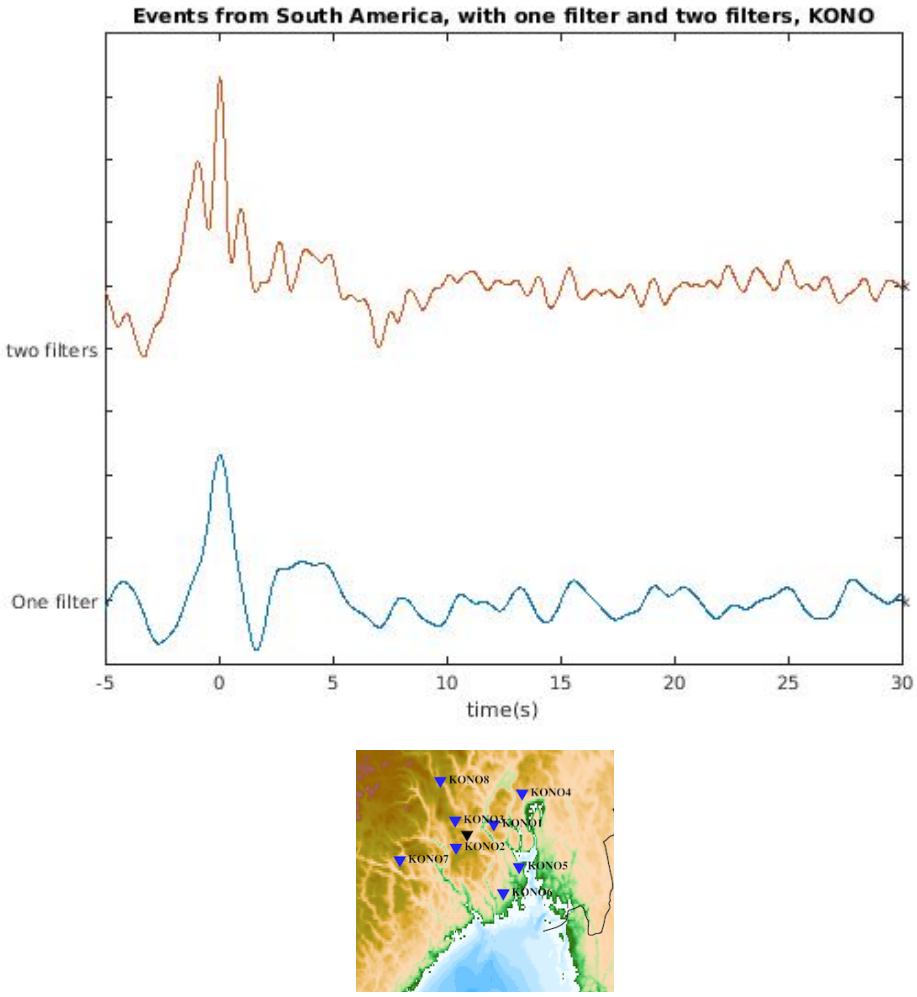

Figure 44: Stacked sections from South America, where one has the same filter as the other three areas, while the second one are filtered twice to remove noise, measured at KONO.

Figure 45 shows the same for KONO1. A clear direct P-wave arrives at 0s in both plots, and the arrival of the Ps-wave at 5s is also clear on both. On the "one filter" plot, there is a positive peak at 12s that is about the same size as the peak at 5s. From 10s-30s on the "two filters" plot there are positive and negative curvatures that show no clear peaks.

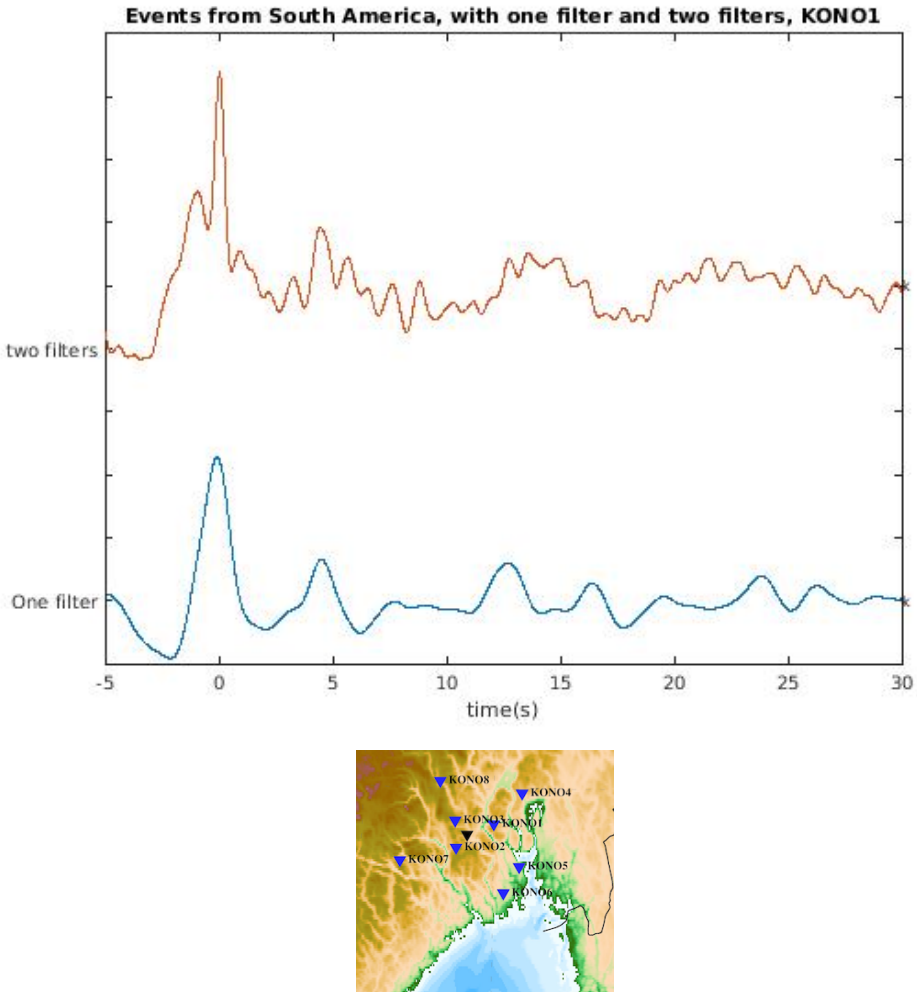

Figure 45: Stacked sections from South America, where one has the same filter as the other three areas, while the second one are filtered twice to remove noise, measured at KONO1.